



Diffusion of halogens (F, Cl, Br, I) in silicic melt

Yves Feisel^{a,*}, Jonathan M. Castro^a, Christoph Helo^a, Anne-Sophie Bouvier^b, Thomas Ludwig^c, Donald B. Dingwell^{d,e}

^a Institute of Geosciences, Johannes Gutenberg-Universität Mainz, 55128 Mainz, Germany

^b Institut des Sciences de la Terre, Université de Lausanne, 1015 Lausanne, Switzerland

^c Institute of Earth Sciences, Universität Heidelberg, 69120 Heidelberg, Germany

^d Department of Earth and Environmental Sciences, Ludwig-Maximilians-Universität München, 80333 Munich, Germany

^e Gutenberg Research College, Johannes Gutenberg-Universität Mainz, 55128 Mainz, Germany

ARTICLE INFO

Associate editor: Sung Keun Lee

Original content: Diffusion of halogens (F, Cl, Br, I) in silicic melts (Original data)
Diffusion of halogens (F, Cl, Br, I) in silicic melts (Original data)

Keywords:

halogens (F, Cl, Br, I)
Diffusion couple
Ionic porosity
Iodine
Silicate melt

ABSTRACT

Chemical diffusion of the halogens F, Cl, Br, and I in silica-rich natural melts was experimentally investigated by the diffusion couple technique. Experiments were conducted under anhydrous conditions at atmospheric pressure and hydrous conditions (~1.5 wt% H₂O) at 160 MPa, over a temperature range of 750–1000 °C and 1000–1200 °C, respectively. Quenched trachytic melt samples were analyzed using an electron microprobe (EPMA) and secondary ion mass spectrometry (SIMS).

All halogens exhibit Arrhenian behaviour during diffusion in the investigated melt compositions with F always diffusing fastest. The other halogens show progressively slower diffusion (F > Cl > Br > I) correlated to their ionic radii. In anhydrous melt a diffusivity range of 3–4 orders of magnitude is covered among the halogens with $D_F(1000\text{ °C}) \sim 5 \times 10^{-13}\text{ m}^2\text{s}^{-1}$ and $D_I(1000\text{ °C}) \sim 1 \times 10^{-16}\text{ m}^2\text{s}^{-1}$. The diffusivities of all halogens increase in hydrous melt with the largest increase being observed for the slowest-diffusing halogens, e.g., resulting in an increase of up to 2 orders of magnitude for iodine at 1000 °C compared to the anhydrous case. This behavior yields a narrower overall diffusive range of only 1–2 orders of magnitude among all halogens. Activation energies (E_A) of diffusion consistently range from ~200 to 390 kJ mol⁻¹ in anhydrous melts. In hydrous melt E_A generally decreases, with the highest decrease determined for F (~131 kJ mol⁻¹) and only slight changes for the other halogens (~201–222 kJ mol⁻¹).

Our diffusivity data of the anhydrous series exhibit a pronounced correlation of diffusivity with the ionic radii, however, this correlation is attenuated in hydrous melt. While in anhydrous melt, halogen diffusion is closely related to ionic porosity, in hydrous experiments, the process of ionic detachment becomes more important as a rate-limiting diffusion mechanism, e.g., comparable to the case of diffusion of divalent/trivalent cations.

The results of this study provide the first consistent diffusion dataset including all halogens under naturally relevant magmatic conditions and highlight the pronounced compositional effect of both, major element and dissolved H₂O on halogen diffusion. The derived diffusion parameters may be readily used for modelling of diffusive fractionation in silicic melts or determining the timescales of natural silicic volcanic processes based on halogen concentration measurements. Furthermore, these data emphasize the potential of diffusive fractionation among the halogens, which may be applied as a monitoring tool for volcanic unrest on actively degassing volcanoes.

1. Introduction

Volatiles are among the most influential chemical constituents of natural silicate magmas. They affect various chemical and rheological melt parameters, which in turn may govern volcanic eruption behavior (Gonnermann and Manga, 2007). Volcanic volatiles are typically

dominated by water (H₂O) and carbon dioxide (CO₂), and sulfur-species (e.g., SO₂), however, the halogen group elements, particularly F and Cl, may also reach significant concentrations (up to few wt.%) in silicic melts and volcanic gases (e.g., Aiuppa et al., 2009; Dolejš and Zajac, 2018). Halogens are known to exert strong effects on the physico-chemical properties of silicate melts, including melt viscosity and

* Corresponding author.

E-mail address: yfeise02@uni-mainz.de (Y. Feisel).

<https://doi.org/10.1016/j.gca.2023.07.008>

Received 28 July 2022; Accepted 10 July 2023

Available online 18 July 2023

0016-7037/© 2023 The Author(s). Published by Elsevier Ltd. This is an open access article under the CC BY license (<http://creativecommons.org/licenses/by/4.0/>).

phase equilibria (e.g., Manning, 1981; Dingwell et al., 1985; Mysen and Virgo, 1985; Dingwell and Hess, 1998; Dolejš and Baker, 2007b; Dolejš and Baker, 2007a; Zimova and Webb, 2007; Giordano et al., 2008; Filiberto et al., 2012; Baasner et al., 2013; Filiberto et al., 2014; Farcy et al., 2016; Webster et al., 2018; Feisel et al., 2022). The physico-chemical effects of added Br and I on silicate melt properties are, by contrast, far less understood. Abundances of Br and I in silicate melt are typically on the order of only few ppb's up to ppms (Aiuppa et al., 2009), consistent with an increasing fluid-melt partition coefficient with increasing ionic radius of Cl (181 pm), Br (196 pm) and I (220 pm) (Bureau et al., 2000). F (133 pm) instead has an ionic radius very similar to O^{2-} and OH^- (140 and 137 pm; Shannon, 1976) and can therefore easily substitute for these components which promotes its compatibility in the melt (Balcone-Boissard et al., 2010).

In addition to melt-property effects, halogens, when outgassed from the magma can have detrimental impacts on the environment and Earth's climate, which include the depletion of stratospheric ozone by Cl and Br (Bobrowski et al., 2003; Bobrowski et al., 2007; von Glasow et al., 2009; Cadoux et al., 2015; Surl et al., 2015; Roberts, 2018). The degassing of F and Cl into isolated pores—aided by the presence of co-exsolved magmatic water—is a key process that relies on the chemical mobility of halogen elements in silicate melt. Indeed, the halogen element diffusion into the vapor phase contributes to the growth of bubbles in silicic lavas and shallow intrusions and may cause etching of silica-rich glass, leading to re-precipitation of vapor-phase cristobalite (e.g., Horwell et al., 2010; Schipper et al., 2020).

Halogens in magmatic systems have received increasing attention in recent years and are routinely measured in volcanic plumes. Because the onset of halogen exsolution occurs at relatively shallow depths compared to the release of H_2O or CO_2 , (e.g., Spilliaert et al., 2006; Lowenstern et al., 2012; Schipper et al., 2019) understanding the rates of halogen diffusion through melt and into bubbles is of utmost importance in interpreting plume gas measurements. Halogen diffusion and exsolution are furthermore expected to be strongly influenced by the presence of magmatic water, even in the small amounts (<wt.%'s) that hydrous components are thought to remain in melt in shallow volcanic conduits. Indeed, halogen measurements at Chaitén (Lowenstern et al., 2012) and Cerdón Caulle (Schipper et al., 2019) show that the release of halogens is inextricable from the release of magmatic water vapor, adding weight to the argument that exsolved halogens are not only shepherded into exsolved bubbles by the action of dissolved H_2O , but are also transported in masses of water vapor. In addition, due to the large general differences in diffusivity between water and most of the halogens (Cl, Br, I; up to several orders of magnitude difference; e.g., Baker et al., 2005), as well as amongst halogens themselves, diffusive fractionation is expected to occur during melt inclusion entrapment or bubble and crystal growth (e.g., Alletti et al., 2007). Relative halogen (or halogen ratios) measurements in volcanic gases and plumes could therefore be applied to track diffusive fractionation processes in order to monitor volcanic activity at depth.

Even though halogen diffusion has been investigated since the 1980s our knowledge is still far from complete. It was shown that halogen diffusion is independent of its concentration and follows Arrhenian behavior in silicate melts. A weak pressure-dependence on diffusivities was reported by some authors (e.g., Dingwell and Scarfe, 1984; Bai and Koster van Groos, 1994), however, most recent studies have found insignificant pressure effects (e.g., Alletti et al., 2007; Balcone-Boissard et al., 2020). Many studies focused on simplified model systems (Dingwell and Scarfe, 1984; Dingwell and Scarfe, 1985; Bai and Koster van Groos, 1994) and those covering natural compositions focused on phonolitic and basaltic systems (Alletti et al., 2007; Balcone-Boissard et al., 2009; Böhm and Schmidt, 2013; Balcone-Boissard et al., 2020), while only few investigated evolved compositions (Fortin et al., 2017; Yoshimura, 2018; Feisel et al., 2019). Most of these studies investigated F and/or Cl diffusion while to date only two studies include Br diffusion (Alletti et al., 2007; Balcone-Boissard et al., 2020) and, to our

knowledge, no study has addressed iodine diffusion. Previous studies have suggested that the diffusivity of the halogens in a highly polymerized melt may be related to the melt's ionic porosity and by this, may be directly correlated with the respective ionic radii of the halogens (e.g., Balcone-Boissard et al., 2020). This relation was not observed in less polymerized melts such as basalts (Alletti et al., 2007). However, none of the previous studies investigated trachytic melt compositions. Moreover, so far no previous study provides data for the behavior of all four halogen species, under hydrous and anhydrous conditions, the data of which highlights the complex interplay of halogen ion characteristics and melt structure. Due to the fact that silicic magma invariably contains H_2O , and that water plays a major role in both the growth of bubbles and transport of co-exsolved halogen species, there is the need for a thorough investigation to aid a detailed understanding of hydrous high-silica melt systems.

In this study we applied the diffusion couple technique to silicic melts synthesized from two natural silicic pumice and lava compositions to determine the diffusivity of all halogens (F, Cl, Br, I) over a temperature range relevant to the studied magmatic systems. Because silicic magmas rise and erupt with significant quantities of magmatic water, both in solution and in the exsolved state, we have conducted anhydrous and hydrous (1.5 wt%) melt experiments to establish a framework to quantify halogen diffusivities and ultimately track halogen degassing during both explosive (e.g., Plinian eruptions like the H3 Hekla event, Weber and Castro, 2017) and long-duration effusive eruptions (e.g., Cerdón Caulle; Castro et al., 2013). Diffusion couples comprising initially step shaped halogen concentration profiles evolved by chemical diffusion during the course of experiments at magmatic P - T -conditions. The resulting dataset greatly improves our understanding of halogen transport mechanisms at crustal conditions and expand the database of halogen diffusion of hydrous magmatic and volcanic environments.

2. Methods

2.1. Experimental procedure

Two different starting materials were used in this study comprising glass synthesized from tephra of the Hekla (Iceland) H3 eruption (e.g., Thordarson and Larsen, 2007; Weber and Castro, 2017), and glass synthesized from natural obsidian lava of the 2011 Cerdón Caulle eruption, Chile (e.g., Castro et al. 2013, 2016; Schipper et al., 2013, 2019; Alloway et al. 2015). The Cerdón Caulle composition was utilized due to limited access to significant quantities of the Hekla material after an initial study on anhydrous halogen diffusion (Feisel et al., 2019). However, because some previously unpublished data on Br and I diffusivities could be derived from the study of the Hekla composition after publication, these data is still included in this study. Furthermore, in order to expand the experiments to hydrous compositions, the highly similar melt composition of Cerdón Caulle was chosen due to its well characterized geochemistry and availability (e.g., Castro et al., 2013). These two starting materials, even though compositionally very similar, derive from quite distinct volcanological environments. While the Hekla material is from a Plinian rhyodacitic eruption, the Cerdón Caulle samples were collected from the other end member of silicic volcanism, that being an effusive system.

The general approaches for the synthesis and experimental methods utilizing the Hekla pumice ("HX" series – "Hekla experiments") and Cerdón Caulle obsidian lava ("CCX" series – "Cerdón Caulle experiments") were the same and are described below.

The initial sample synthesis was carried out in the laboratories of the Earth Science department of the LMU Munich. Natural pumice (HX) or obsidian lava (CCX) was respectively crushed and melted in a Pt crucible using a Nabertherm muffle furnace at 1450 °C. After the crucible was full, it was transferred to a Nabertherm elevator furnace and synthesized at high temperature (1400–1550 °C) for ~2 days to produce almost completely volatile-free glass. To accelerate devolatilization and melt

homogenization, the melts were stirred by a rotating Pt-rod attached to a rheometer. The rheometer was additionally used to identify the bulk loss of volatiles which was indicated by a steady-state plateau of the torque reading over time. After the first synthesis, the crucible was set on an insulation to cool at room temperature and the batch was crushed and split afterwards. One half was enriched with halogen-bearing Na-salts (NaF, NaCl, NaBr, NaI) so that each halogen would account for approximately 1 wt% of the whole batch after mixing, aiming to yield a total of 4 wt% halogens in the resulting starting material. The halogen-depleted split was in turn enriched with a certain amount of Na₂CO₃ to account for the sodium enrichment in the halogen-bearing glass, due to the use of aforementioned Na-salts to add halogens. Each aliquot was again synthesized and homogenized at temperatures of 1450–1550 °C for up to four days, again utilizing the elevator furnace and rheometer setup for improved homogenization. From the resulting glass aliquots ca. 2 mm thick polished glass discs (4.6 mm diameter) were prepared for anhydrous experiments while the remaining glass was crushed to powder to be used in hydrous diffusion experiments.

Due to the synthesis being run at atmospheric pressure in an open furnace, some halogen loss was expected to occur during the second synthesis step. The final starting glasses did indeed show strong halogen loss (Table 1). However, the halogen contents in the enriched starting materials were still significantly enriched compared to the depleted aliquots and could therefore be utilized for diffusion couple experiments. The glasses were mostly homogeneously enriched in halogens within the same batch which was subsequently confirmed by concentration vs. distance analyses of diffusion couple samples.

2.1.1. Anhydrous diffusion experiments

Diffusion couples were constructed using 5 mm platinum tube with a wall thickness of 0.2 mm. The bottom of the capsule was closed with a Pt lid which was pressed onto and welded to the tube using an arc-welder. Afterwards the bottom of the capsule was tamped into a cylindrical shape. One halogen-enriched glass disc was loaded into the bottom of the capsule and a disc of the equivalent halogen-depleted glass was loaded on top of it, resulting in both pieces touching at their polished surfaces. Each capsule was closed by welding a second lid to the top of

Table 1

Major element composition of the synthesized starting glasses as determined by EPMA and SIMS analysis. All values represent units of wt.% unless otherwise stated. All data are corrected for Na-loss during EPMA analysis. Absolute values of Br and I estimated based on SIMS analyses.

	HX ^a		CCX	
	Enriched (n = 15)	Depleted (n = 14)	Enriched (n = 6)	Depleted (n = 5)
SiO ₂	68.5 (4)	68.3 (3)	67.8 (3)	67.9 (5)
TiO ₂	0.46 (2)	0.46 (2)	0.66 (3)	0.67 (2)
Al ₂ O ₃	14.7 (1)	14.57 (8)	14.49 (4)	14.48 (7)
FeO	4.6 (3)	4.76 (6)	3.84 (5)	3.94 (8)
MgO	0.46 (2)	0.44 (2)	0.60 (3)	0.62 (2)
MnO	0.13 (2)	0.15 (2)	0.12 (4)	0.11 (2)
CaO	2.85 (7)	2.82 (5)	2.11 (3)	2.12 (3)
Na ₂ O	6.2 (2)	6.35 (7)	6.9 (1)	7.8 (1)
K ₂ O	2.10 (3)	2.20 (3)	2.39 (3)	2.65 (4)
F	0.53 (2)	0.04 (3)	0.96 (2)	0.03 (1)
Cl	0.26 (1)	0.02 (2)	0.4 (1)	0.04 (1)
Br	nd	nd	~ 2500 ppm	~ 1 ppm
I	nd	nd	~ 290 ppm	0
Total	100.52	100.05	99.82	100.35
NBO/ T ^b	0.08	0.08	0.09	0.11
Tg ^c (°C)	633	681	589	657

^a Data from Feisel et al. (2019).

^b NBO/T is calculated after (Mysen, 1988) and Giordano et al. (2008).

^c Tg is calculated using the spreadsheet of Giordano et al. (2008).

the capsule, which ensured closed-system conditions. The diffusion experiments were carried out in a vertical tube furnace at atmospheric pressure. Each capsule was first weighed and then loaded into an alumina tube that is closed on the bottom end, making sure the halogen-depleted half was facing upwards. After the furnace equilibrated at the target temperature the alumina tube was inserted vertically into the furnace through a small opening in the top, ensuring that the capsule was sitting upright on the closed bottom of the alumina tube in the hot zone of the furnace. The temperature was monitored by the internal thermocouple and an external K-type thermocouple being in direct contact with the experimental capsule. Additionally, several experiments were monitored using a second external K-type thermocouple interfaced with an Arduino microprocessor to read the temperature remotely and store the *P-T-t* data to a computer. Temperatures are estimated to be accurate to ±2 °C based on the manufacturer's (*Omega*) reported accuracy of the thermocouple device. The experimental durations ranged from ~20 h to 35 days depending on the temperature investigated. The time needed for the capsule to heat to the target temperature ranged between 3 and 5 min. The experiments were quenched by sliding the alumina tube out of the hot furnace and letting it cool in air at room temperature in an upright position. Typical cooling times to a temperature of 200 °C as indicated by the external thermocouple were in the range of 3–4 min. The comparably short heating and quenching times are considered to have no significant effect on the final diffusion profiles and were therefore not corrected for during diffusion coefficient calculation.

2.1.2. H₂O-bearing diffusion experiments

Hydrous experiments were carried out using CCX starting material only and are denoted by "CCX-H". The capsule preparation followed the procedure described in Feisel et al. (2022) using powdered starting glass and Pt-tube with a diameter of 4 mm and a wall thickness of 0.2 mm as capsule material. After welding the capsule shut on the bottom and tamping into a cylindrical shape using a tight-fitting rod, ground glass powder of the halogen-enriched samples was introduced until the capsule was filled about halfway. During filling the powder was slightly tamped several times to avoid entrapment of air and ensure a flat diffusion interface. The exact amount of added sample powder was weighed using an analytical balance of 5-digit precision and the equivalent amount of 1.5 wt% H₂O was added to the capsule using a microsyringe. This water content was chosen as it is broadly representative of intermediate H₂O contents during the 2011 eruption of Cordón Caulle (0.1–4 wt%; e.g., Schipper et al., 2019) and is moreover relevant to processes in typical shallow volcanic conduits, where critical processes such as degassing take place. The procedure was repeated using the halogen-depleted powder and again the equivalent amount of 1.5 wt% H₂O for the top part of the capsule. Finally, the capsule was closed by welding a tight-fitting lid to the open end and tamped into cylindrical shape with a pressure of ~750 kg using a hydraulic press. Before an experiment, the capsules were repeatedly heated to ~120 °C and weighed to confirm no weight loss. Capsules with significant weight loss were discarded.

Experiments were performed in a *Deltech* vertical tube furnace fitted with a gas-pressurized TZM (Tungsten Zirconium Molybdenum) cold-seal pressure vessel assembly. The sample capsule is loaded into the cold-seal assembly which is connected to a stainless-steel high-pressure tubing using Argon gas as a pressure medium. To mitigate water-loss from inside the capsule to the Ar-atmosphere ca. 0.3 MPa of CH₄ was inserted to the pressure system before pressurizing with Ar (e.g., Sisson and Grove, 1993; Szramek et al., 2006; Shea and Hammer, 2013). The cold-seal assembly consists of an inner autoclave made of TZM (~30 mm outer, ~6.5 mm inner diameter) and an outer sheath made of Inconel (~50 mm diameter, 5 mm wall thickness), both attached to a water-cooled base on the bottom. The space between the sheath and autoclave is constantly purged with Ar during the experiment to provide a non-reactive atmosphere for the inner pressurized autoclave. A second,

lower vessel made of stainless steel is attached to the bottom of the water-cooled coupling base and is connected to the pressure line. The sample capsule sits in a small cup which in turn is attached to the top of an Inconel rod. The position of the rod in the assembly can be controlled from the outside using a neodymium ring magnet. The whole assembly is inserted into the vertical tube furnace from the bottom before it is brought up to the target temperature and pressure. The pressure is generated by an HIP GB-60 gas booster device operated with compressed air and conveying Ar gas as a pressurizing medium.

During the time of heating, the capsule remains in the water-cooled part of the assembly (rapid-quench coupler) which is outside the furnace and constantly flushed with water (~15 l/min). When the target *P-T* conditions are reached and equilibrated, the experiment is started by upward movement of the sample holder which brings the capsule—within seconds—into the hot zone of the furnace. Quenching is done the opposite way by sliding the magnet down to bring the capsule back into the water-cooled zone of the assembly, resulting in an almost immediate quench. During the experiments, temperature is monitored using the internal thermocouple of the furnace and an external K-type thermocouple which is inserted into a small bore in the sheath of the TZM assembly and touching the top of the internal autoclave. The pressure is monitored with a factory-calibrated Bourdon-tube gauge and a digital pressure transducer. Considering the small thermal volume of the capsule relative to the massive TZM autoclave we expect no significant thermal gradient within the diffusion couple capsule.

Upon the start of the experiment while inserting the rod with the sample capsule into the hot zone of the autoclave, a pressure drop of up to 20 MPa over ca. 10 s is commonly observed. We interpret this to occur due to the displacement and concomitant cooling of a large amount of the hot gas from the autoclave to the cooler parts of the pressure system during the insertion of the rod. The rod is cold relative to the hot atmosphere in the autoclave and upon heating causes the pressure to increase again slowly by typically about 10 MPa over the duration of ca. 50 s. The opposite process is observed upon quench of the experiment, resulting in an up to 20 MPa overpressure during quench, which decreases to ca. 10 MPa overpressure in about 50 s at the end of an experiment. These processes are accounted for by slight overpressurization before the start of the experiment. The pressure increase at the end of the experiment also ensures that bubble formation is suppressed during the quench. Additionally, it was shown that halogen diffusion is mostly insensitive to pressure variations (e.g., Baker and Balcone-Boissard, 2009). Therefore, we consider these short-lived pressure fluctuations to be insignificant for the results of the diffusion experiments.

2.2. Analytical methods

Before preparation for further analyses all samples were weighed individually to ensure no weight loss or gain occurred during the experiment. Diffusion couple capsules were embedded in epoxy and cut open along the centre of the capsule and parallel to the diffusion direction (i.e., parallel to the cylindrical capsules rotation axis) using a Buehler IsoMet precision saw. All samples were polished using a series of diamond embedded disks to an ultimate grain size of 1 µm while taking care that the polished surface remained parallel to the diffusion direction.

2.2.1. Electron probe micro analysis (EPMA)

Major element and halogen concentration analyses of experimental glasses were conducted at the Department of Geoscience of the University of Mainz, and using a JEOL JXA8200 electron microprobe. Analyses employed an acceleration voltage of 15 kV, a beam current of 12 nA, and a beam diameter of 10 µm. Dwell times for F and Cl were 120 s and 30 s, respectively, yielding a detection limit of 60 ppm (1σ). Analysis dwell times of each major element was: Si 25 s, Al 40 s, Na 20 s, K 30 s, Ca 30 s, Fe 60 s, Mg 30 s, Mn 50 s, and Ti 30 s. The device was calibrated

before a measurement using the following reference materials: SrF₂ (F), tugtupite (Ca, Na), VG-2 (Ca, Mg), VG-A99 (Fe, Si), MnTi (Mn, Ti), and orthoclase (Al, K). Proper calibration was assessed by analyzing standards VG-2, VG-A99, VG-568 and a natural obsidian standard (~74 wt% SiO₂) repeatedly during each analytical session. The data was corrected using the ZAF method.

Concentration vs. distance profiles were acquired using line-scans with a fixed step-width of 5–250 µm depending on the sample (i.e., the anticipated diffusive speeds and therefore profile distances) and the position of the analyzed points relative to the diffusion interface. Points in the transition zone between the two diffusion couple halves were analyzed using a smaller step-width while the profile ends were covered by a larger step-width. The achievable resolution according to the beam diameter was on the order of 10 µm, which was significantly less than the length of the shortest profiles analyzed by EPMA (Cl; typically >50–100 µm). Profiles were acquired along traverses away from the capsule edges to avoid analyzing inhomogeneities that could distort diffusion profile data (e.g., devitrification, Feisel et al. 2019) and most samples were analyzed along different traverses to confirm sample homogeneity.

2.2.2. Secondary Ion Mass Spectrometry (SIMS)

As the concentration of Br and I in the samples is too low to be reliably detected by EPMA, experimental samples were further analyzed on the SIMS. The analyses of all HX samples and of CCX1 and CCX4 were carried out during two analytical sessions in October 2018 and January 2019 at the University of Lausanne, Switzerland. The other samples (CCX3, CCX5 and all CCX-H) were analyzed at Heidelberg University, Germany, in two sessions in May 2021 and April 2022. Both facilities feature a CAMECA IMS 1280HR ion microprobe. The analytical parameters for all SIMS analyses (halogens and H₂O) in both labs are summarized in Table S1 of the supplementary material. The effective spatial resolution of SIMS analyses was different during the different analytical sessions. In Lausanne, a resolution of ~14 µm was used while ~5 µm could be achieved in Heidelberg for halogen analyses (Table S1). Water analyses carried out in Heidelberg were run with a spatial resolution of ~10 µm.

Analyses carried out at the University of Lausanne were referenced internally on each sample in an area far outside of the region of diffusion where the constant Si-content was known from EPMA analyses. These data included the less abundant Si-isotope ³⁰Si for calculation of ratios with Br and I which are of low concentration in our samples compared to F and Cl. ²⁸Si and ¹⁹F intensities were detected using a Faraday-Cup. The other halogens (³⁵Cl, ^{79/81}Br, ¹²⁷I) and ³⁰Si were analyzed using electron multipliers.

The SIMS analyses of halogens in Heidelberg were calibrated using an obsidian glass (JV1, Pichavant, 1987) for F and Cl and the GSE-1G glass for Br and I (Marks et al., 2017a; Marks et al., 2017b; Wiedenbeck, 2017). The accuracy of these analyses is limited by the poor homogeneity of halogens in GSE-1G and the fact that JV1 is not an established reference material with multiple independent determinations of the concentrations. The halogen concentrations determined by SIMS must therefore be interpreted as semi-quantitative with an estimated accuracy of ≤50 % (relative error).

For each water-bearing sample (CCX-H), H₂O concentration profiles were acquired next to the halogen profiles using a CAMECA IMS3f ion microprobe at Heidelberg University. The H₂O background caused by in-situ contamination was reduced by using a LN₂-cooled metal plate in the sample chamber. The apparent H₂O concentration caused by in-situ contamination was monitored by analyzing San Carlos olivine and was <0.01 wt%. H₂O analyses were calibrated using JV1 as reference material. Accuracy is estimated to be <20 % relative error.

3. Results

3.1. Chemical composition of starting materials

The major element compositions of the different starting materials as determined by microprobe analyses are compiled in Table 1. The synthesized samples reveal a similar composition, both plotting in the field of trachyte in a TAS diagram, very close to the borders to rhyolite and dacite. However, the CCX melt is slightly enriched in alkalis (Na_2O , K_2O) compared to the HX melt. All samples were analyzed using line scans on the microprobe not only to measure F and Cl gradients but also to validate major element homogeneity over the diffusion couple (Fig. 1). Maximum absolute concentrations of F are around 0.5–0.6 wt% in the HX samples, and about 0.8–1 wt% in the CCX samples. Cl concentrations are about 0.2–0.3 wt% in the HX samples and about 0.3–0.4 wt% in the CCX samples. Absolute Br and I concentrations were only measured for the CCX samples using the SIMS at Heidelberg University. The maximum Br and I concentrations in the halogen-enriched glasses of the CCX melts are ~2500 ppm and ~300 ppm, respectively.

The liquidus temperatures of the starting materials at atmospheric pressures was not determined experimentally in the scope of this study. However, the studies of Castro et al., (2013) and Weber and Castro (2017) provide experimental phase-petrology data of the starting materials used here. For the Cordon Caille obsidian Castro et al. (2013) found water-saturated liquids in the temperature range of 950–975 °C depending on the pressure. Likewise, the study of Weber & Castro (2017) found that, with the *P-T* conditions applied, they could not reproduce liquidus conditions up to temperatures of 1000 °C, even though the experiments were also water-saturated. The recent anhydrous diffusion experiments are therefore expected to have taken place at sub-liquidus conditions. Most importantly, the experimental conditions were all well above the calculated glass transition temperature (T_g ; Table 1).

3.2. Post-experimental diffusion couple textures

During data acquisition, all diffusion couples were assessed for textural homogeneity by means of backscattered electron images (Figs. S5–S8). Most samples comprised a clean and straight diffusion interface between two homogeneous glassy areas which were particularly prominent in the anhydrous samples. Few anhydrous samples developed minor bubbles on the diffusion interface which were interpreted to stem from air entrapment during sample preparation. Some samples and mainly those of the hydrous series contained cracks in the glass, which were interpreted to stem from the relatively fast quenching rates (Figs. 2a, S7). However, the cracks were not found to influence the acquired diffusion data. Few samples underwent deformation during the experiments caused by severe bubble formation or the onset of convection. Both phenomena were mostly recognized in experiments of the water-bearing series in which the melt viscosity was reduced due to the presence of water (e.g., Giordano et al. 2008) which enhanced convection. These effects resulted in distorted diffusion couple geometry, and according samples were discarded from further analysis (Fig. S8). Most water-bearing samples contained minor bubbles after the experiments which were found to have no significant effect on the halogen diffusion profiles (Fig. S7). Some of the samples of the anhydrous series contained minor crystals and/or areas of devitrified glass, especially close to the diffusion interface (e.g., Fig. S5f). These areas were avoided during data acquisition. Small amounts of oxide phases (<100 μm ; <1 vol%) were recognized in the halogen-bearing parts of some experiments utilizing the CCX melt. These were analyzed qualitatively using EDS which showed they are tungsten-oxides. This was interpreted to stem from a slight contamination of the sample powder caused by using a tungsten-carbide mill for sample preparation. However, these oxides are not thought to affect halogen diffusion in our experiments.

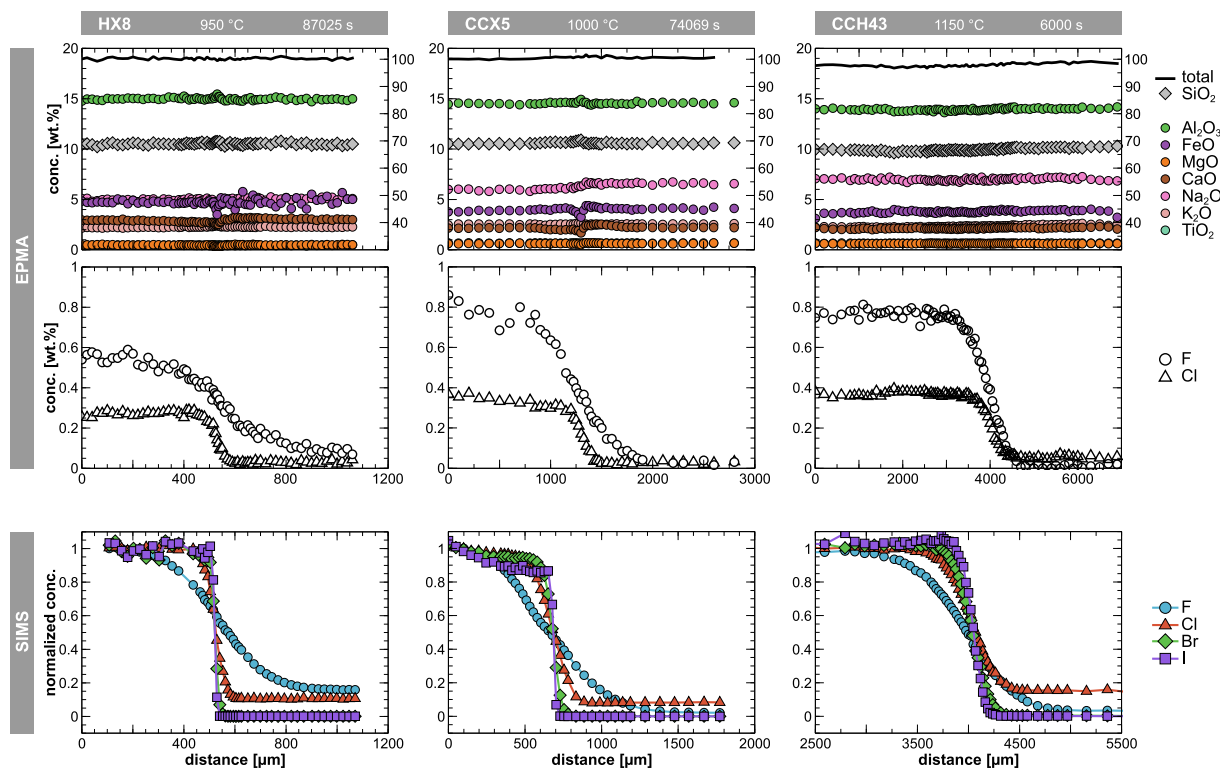


Fig. 1. Concentration vs. distance diagrams of one sample of each investigated melt composition acquired by EPMA and SIMS analyses. In the upper row, data of SiO_2 and totals refer to the secondary y-axis. EPMA data represents absolute values whereas the SIMS data was normalized to the average of the 4 outermost datapoints of each respective halogen in the enriched diffusion couple half. This way it is possible to visualize all halogens of a sample in one diagram.

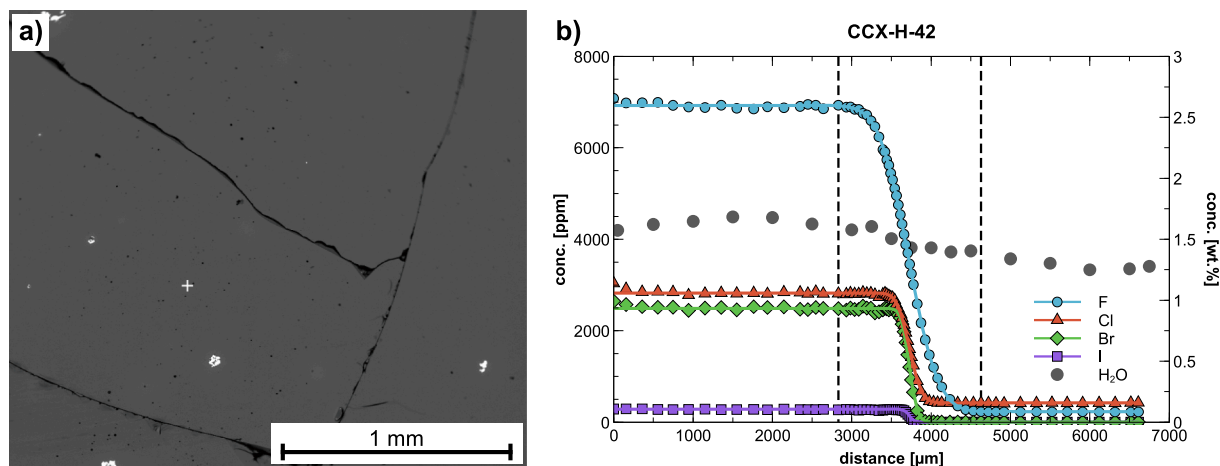


Fig. 2. Backscattered image and diffusion profiles of sample CCX-H-42. (a) Backscattered image of the center part of sample CCX-H-42 showing minor cracks caused during rapid quench (few seconds). (b) Concentration vs. distance profiles of F, Cl, Br, I and H₂O as acquired by SIMS. The halogen data are plotted together with their respective fit curves calculated using Eq. (1). Diagrams of the other CCX-H samples are provided in the supplementary material (Fig. S1).

3.3. Halogen diffusion coefficients

Most concentration profiles comprise a smooth and symmetric transition between the high and low halogen concentration portions of the charge, indicating that no other processes than diffusion (e.g., convection) were involved (Fig. 1). Smooth and symmetric profiles are recognized especially for experiments run at high temperatures. Diffusion profiles of Br and I are in general shorter than those of F and Cl and some diffusion profiles showed inhomogeneous initial Br and I concentrations on the high concentration side of the diffusion couples. These are attributed to slight heterogeneities in the starting material and therefore only occur in experiments of the anhydrous series (e.g., HX7). However, all concentration vs. distance profiles presented here yielded good results during fitting and are treated as effective binary diffusion of each halogen element in the melt matrix (e.g., Zhang 2010).

Diffusion coefficients for each acquired concentration vs. distance profile were calculated by fitting the respective data to the equation for constant one-dimensional diffusivity between two semi-infinite media (Crank, 1975):

$$C(x, t) = \frac{C_{low} + C_{high}}{2} + \frac{C_{low} - C_{high}}{2} \operatorname{erf}\left(\frac{x - x_0}{2\sqrt{Dt}}\right) \quad (1)$$

The parameter $C(x, t)$ describes the concentration at distance x (m) after the experimental time t (s). C_{low} (ppm) is the concentration of the halogen-poor, and C_{high} (ppm) the concentration of the halogen-rich half-space. The term erf indicates the error function. x_0 (m) describes the position of the diffusion interface and is in this case determined mathematically. The variable D (m²/s) is the diffusion coefficient.

Data fitting was performed using the nonlinear least-squares method implemented in a *MATLAB* script, specifically programmed for easy use with diffusion profile data. The results obtained by this script were regularly validated by comparing to the results calculated by the commercially available curve-fitting software *CurveExpertPro*. As Eq. (1) is independent of absolute concentrations it was used with both, concentration data determined by EPMA and SIMS and ratios of halogen-over silica-concentration (e.g., ¹⁹F/²⁸Si) as determined by SIMS to calculate diffusion coefficients. All parameters of Eq. (1) except x and t were calculated based on the fitting algorithm. In some cases, parameters C_{low} and C_{high} were set manually to facilitate proper fitting calculations. For example, sample CCX5 was initially analyzed across an insufficient distance to resolve both far-field concentration plateaus of the F concentration profile (Fig. S3g). Therefore, a third, longer EPMA analysis was carried out that incorporates the enriched and depleted plateaus and the obtained concentrations were set manually during the

fitting process of the shorter F concentration profiles. Additionally, some profiles suffered from slight distortion, caused, for example, by deformation of the capsule during quench, and resulting in asymmetrical profiles which was mainly prominent in the longest profiles of F diffusion. Where profiles were asymmetrical, each half of the diffusion profile was fitted individually using Eq. (1) and the results were compared to those of the complete profile. Those profiles of which the individually fitted halves yielded different diffusion coefficients larger than 0.6 orders of magnitude were discarded. F diffusion coefficients calculated on profiles where this method was applied are indicated by “*” in Table 2. Typical concentration vs. distance profiles of sample CCH-X-42 fitted with Eq. (1) are illustrated in Fig. 2b. All measured diffusion profiles with their respective fit curves are provided in Figs. S1–S4 of the supplementary material.

All diffusion profiles of the typically slower diffusing Br and I were assessed for effects of convolution using the software *PACE* (Jollands, 2020) including the respective analytical parameters (Table S1). Due to the larger resolution used by the SIMS in Lausanne (14 μm), most of the profiles of the HX series suffered from convolution effects for which these profiles were corrected. During assessment with *PACE* some profiles revealed that barely any diffusion had occurred during the course of the experiment. These data were discarded from further diffusion coefficient calculations (e.g., HX9; Table 2).

Some of the analysed profiles revealed anomalous major element concentration gradients close to the diffusion interface reminiscent of pattern typically associated with uphill diffusion (e.g., FeO in sample CCX 5 of Fig. 2). These features indicate that cross-diffusivities of some components may have been present during the experiments (e.g., Zhang, 2010) which may have affected the results. However, the halogen diffusion profiles do not show any signs of distortion on the order of the length scales of the major element inhomogeneities. Nevertheless, slight effects of cross-diffusivities between the matrix and halogens cannot completely be ruled out in the present experiments.

3.3.1. Anhydrous HX

Of the nine HX experiments presented in Feisel et al. (2019), six samples were analyzed by SIMS for the scope of this study. One concentration vs. distance profile was acquired for each of the samples, covering lengths of ~500–1000 μm. Diffusivities of F and Cl determined here agree well with the results of microprobe analyses indicating that F is generally faster than Cl by up to 2 orders of magnitude in the investigated temperature range. D values are on the order of 10⁻¹⁵–10⁻¹³ m²/s for fluorine and 10⁻¹⁷–10⁻¹⁵ m²/s for chlorine, of which the lower and higher values each correspond to temperatures of 750 °C (HX9) and 950

Table 2

Conditions and results of all experiments. Those of the anhydrous series (HX and CCX) were carried out at $P = 1$ bar. Hydrated experiments were done at $P = 160$ MPa. All diffusivities in m^2/s . The standard errors (SE) are derived from the least-squares diffusion profile fitting.

sample	T [°C]	t [s]	H ₂ O [wt. %]	#	D_F	SE	D_{Cl}	SE	D_{Br}	SE	D_I	SE
HX9	750	3,023,535	–	1 ^a	1.6×10^{-15}	2.2×10^{-16}	1.7×10^{-17}	4.3×10^{-18}				
				2 ^b	$1.6 \times 10^{-15*}$	1.6×10^{-16}	3.9×10^{-17}	5.6×10^{-18}				
HX7	800	587,235	–	1 ^a	6.6×10^{-15}	7.9×10^{-16}	4.9×10^{-17}	7.3×10^{-18}				
				2 ^a	1.1×10^{-14}	9.9×10^{-16}	1.6×10^{-16}	2.1×10^{-17}				
				3 ^b	1.1×10^{-14}	3.1×10^{-16}	4×10^{-16}	3.2×10^{-17}				
HX3	850	171,502	–	1 ^a	1.6×10^{-14}	2.6×10^{-15}	3.9×10^{-16}	1.0×10^{-16}				
				2 ^a	1.9×10^{-14}	3×10^{-15}	4.5×10^{-16}	1.2×10^{-16}				
				3 ^b	$2.3 \times 10^{-14*}$	2.3×10^{-15}	4.3×10^{-16}	5×10^{-17}	4.1×10^{-17}	1.5×10^{-17}	1.3×10^{-17}	1.1×10^{-17}
HX10	850	266,855	–	1 ^a	1.9×10^{-14}	2.2×10^{-15}	3.9×10^{-16}	6×10^{-17}				
				2 ^a	2×10^{-14}	2.6×10^{-15}	7.4×10^{-16}	2×10^{-16}				
				3 ^b	$2.1 \times 10^{-14*}$	9.1×10^{-16}	6.2×10^{-16}	3.8×10^{-17}				
CCX3	850	237,370	–	1 ^a	$6.6 \times 10^{-14*}$	6.5×10^{-15}	2.4×10^{-15}	4.6×10^{-16}				
				2 ^b	$3.6 \times 10^{-14*}$	6×10^{-15}	3.5×10^{-15}	3.6×10^{-16}				
CCX4	900	170,880	–	1 ^a	$6.3 \times 10^{-14*}$	6.3×10^{-15}	1.7×10^{-15}	2.5×10^{-16}				
				2 ^a	$6.6 \times 10^{-14*}$	5.8×10^{-15}	5.7×10^{-15}	6.2×10^{-16}				
				3 ^b	5.4×10^{-14}	5.3×10^{-15}	9.7×10^{-15}	7.3×10^{-16}	1.2×10^{-15}	6.3×10^{-17}	1.8×10^{-16}	3×10^{-17}
CCX1	950	82,770	–	1 ^a	$1.1 \times 10^{-13*}$	8.3×10^{-15}	8.8×10^{-15}	6.4×10^{-16}				
				2 ^a	$1.2 \times 10^{-13*}$	9.9×10^{-15}	7.1×10^{-15}	6.4×10^{-16}				
				3 ^b	$1.1 \times 10^{-13*}$	7.2×10^{-15}	7.7×10^{-15}	3.8×10^{-16}	1.1×10^{-15}	6.5×10^{-17}	2.5×10^{-16}	5.4×10^{-17}
CCX5	1000	74,069	–	1 ^a	6.9×10^{-13}	3×10^{-14}	4×10^{-14}	3×10^{-15}				
				2 ^a	5×10^{-13}	2.1×10^{-14}	5.8×10^{-14}	4.2×10^{-15}				
				3 ^a	6.4×10^{-13}	7.3×10^{-14}	6.7×10^{-14}	1.2×10^{-14}				
				4 ^b	6.7×10^{-13}	3.8×10^{-14}	7.0×10^{-14}	1.3×10^{-14}	1.3×10^{-14}	3.8×10^{-15}		
				5 ^b	7.5×10^{-13}	2.2×10^{-14}	7.3×10^{-14}	2.2×10^{-15}	1.2×10^{-14}	6.4×10^{-16}	9.4×10^{-16}	6.5×10^{-17}
CCX-H-38	1000	16,380	1.9 (1)	1 ^a	3.3×10^{-12}	2.2×10^{-13}	4.3×10^{-13}	7.3×10^{-14}				
				2 ^b	3.3×10^{-12}	7.9×10^{-14}	5.4×10^{-13}	1.9×10^{-14}	2.5×10^{-13}	8×10^{-15}	9.4×10^{-14}	4.1×10^{-15}
CCX-H-40	1050	10,200	1.9 (1)	1 ^a	6.2×10^{-12}	4.9×10^{-13}	9.2×10^{-13}	1.1×10^{-13}				
				2 ^b	6.6×10^{-12}	1.3×10^{-13}	1.3×10^{-12}	7×10^{-14}	5.8×10^{-13}	2.8×10^{-14}	2.3×10^{-13}	1.5×10^{-14}

(continued on next page)

Table 2 (continued)

sample	T [°C]	t [s]	H ₂ O [wt. %]	#	D _F	SE	D _{Cl}	SE	D _{Br}	SE	D _I	SE
CCX-H-42	1100	8100	1.5 (1)	1 ^a	5.5 × 10 ⁻¹²	3.9 × 10 ⁻¹³	7.9 × 10 ⁻¹³	8.1 × 10 ⁻¹⁴				
				2 ^b	5.3 × 10 ⁻¹²	6.6 × 10 ⁻¹⁴	9.5 × 10 ⁻¹³	4.1 × 10 ⁻¹⁴	4.2 × 10 ⁻¹³	1.9 × 10 ⁻¹⁴	1.6 × 10 ⁻¹³	1.2 × 10 ⁻¹⁴
CCX-H-43	1150	6000	2.1 (2)	1 ^a	1.3 × 10 ⁻¹¹	7 × 10 ⁻¹³	4.2 × 10 ⁻¹²	3.4 × 10 ⁻¹³				
				2 ^b	1.3 × 10 ⁻¹¹	2.3 × 10 ⁻¹³	3.6 × 10 ⁻¹²	1.2 × 10 ⁻¹³	1.6 × 10 ⁻¹²	4.8 × 10 ⁻¹⁴	6.5 × 10 ⁻¹³	3.4 × 10 ⁻¹⁴
CCX-H-44	1200	4800	2.0 (2)	1 ^a	1.9 × 10 ⁻¹¹	1 × 10 ⁻¹²	7.6 × 10 ⁻¹²	6.6 × 10 ⁻¹³				
				2 ^b	2 × 10 ⁻¹¹	5.4 × 10 ⁻¹³	7.7 × 10 ⁻¹²	4.3 × 10 ⁻¹³	3.9 × 10 ⁻¹²	2.4 × 10 ⁻¹³	2.1 × 10 ⁻¹²	2.1 × 10 ⁻¹³
HX5	900	154,560	–	1 ^a	4.7 × 10 ⁻¹⁴	3.4 × 10 ⁻¹⁵	1.0 × 10 ⁻¹⁵	1 × 10 ⁻¹⁶				
				2 ^a	4.6 × 10 ⁻¹⁴	4.6 × 10 ⁻¹⁵	8.7 × 10 ⁻¹⁶	9.8 × 10 ⁻¹⁷				
				3 ^b	3.2 × 10 ^{-14*}	3.1 × 10 ⁻¹⁵	1.0 × 10 ⁻¹⁵	6.8 × 10 ⁻¹⁷	9.6 × 10 ⁻¹⁷	3.3 × 10 ⁻¹⁷		
HX8	950	87,025	–	1 ^a	1.3 × 10 ⁻¹³	1.3 × 10 ⁻¹⁴	4.5 × 10 ⁻¹⁵	5.6 × 10 ⁻¹⁶				
				2 ^a	1.1 × 10 ⁻¹³	1.5 × 10 ⁻¹⁴	1.5 × 10 ⁻¹⁵	3.4 × 10 ⁻¹⁶				
				3 ^b	1.4 × 10 ⁻¹³	7.3 × 10 ⁻¹⁵	5.9 × 10 ⁻¹⁵	4.5 × 10 ⁻¹⁶	1.3 × 10 ⁻¹⁵	1.4 × 10 ⁻¹⁶	2.7 × 10 ⁻¹⁶	9.6 × 10 ⁻¹⁷

^a Results from EPMA analyses. EPMA data of HX series from Feisel et al. (2019).

^b Results from SIMS analyses; data in italics was corrected for convolution effects using “PACE” (Jollands, 2020).

* Asymmetric profiles were first fitted each half at a time to confirm reliability of the fit of the complete profile (see text for further discussion).

°C (HX8), respectively (Table 2). Bromine and iodine diffusivities are generally lower than those of chlorine, with Br consistently being faster than I. D_{Br} ranges from 10⁻¹⁷ to 10⁻¹⁵ m²/s while D_I values are about half an order of magnitude smaller at the corresponding temperatures, ranging from ca. 10⁻¹⁷ to 10⁻¹⁶ m²/s (Table 2).

3.3.2. Anhydrous CCX

Out of seven anhydrous experiments performed using CCX melt and analyzed by EPMA, three were discarded due to textural features indicating compromised geometry. The remaining four experiments were additionally analyzed by SIMS. Diffusivities of all halogens in samples using the CCX melt are similar to those obtained for the HX melt. However, the difference between F and Cl diffusion is less pronounced in this melt composition compared to HX. Diffusion coefficients of F (D_F) range from ~10⁻¹⁴ to 10⁻¹³ m²/s in the temperature range of 850 °C (CCX3) to 1000 °C (CCX5). Cl diffusion is up to two orders of magnitude slower with ~10⁻¹⁷ to 10⁻¹⁴ m²/s at these temperatures. For these two halogens, results of EPMA and SIMS analyses agree well within statistical errors (Table 2). Diffusion of Br is slower than that of Cl by ~0.5–1.5 orders of magnitude and I is even slower than Br by ~1 order of magnitude with diffusivities in the range of ~10⁻¹⁵–10⁻¹⁴ and ~10⁻¹⁶ m²/s, respectively.

3.3.3. Hydrous CCX-H

All diffusion couple experiments of the hydrous series performed in the TZM assembly were analyzed both by EPMA (F, Cl) and by SIMS (F, Cl, Br, I). In general, diffusivities are higher than those obtained for the anhydrous CCX series with D_F ranging from ~10⁻¹² to ~10⁻¹¹ m²/s from 1000 to 1200 °C. Cl diffusion is 0.5 to 1 orders of magnitude slower than F, and Br and I are even slower. However, diffusivities of Cl, Br and I are all within less than one order of magnitude of each other at the respective experimental temperatures (Table 2). This results in a total diffusivity range of only 1–2 orders of magnitude among all halogens

which is significantly less than observed for the anhydrous series of CCX melt which spans a range of 3–4 orders of magnitude among all halogens (Table 2).

3.4. Temperature dependence of halogen diffusion

All diffusion coefficients determined in this study increase with increasing temperature for each of the used melt compositions. As shown in various previous studies, diffusivity follows Arrhenian behavior (e.g., Baker and Balcone-Boissard 2009), which is also confirmed by our data. Plotted in a diagram of log(D) vs. inverse temperature (Fig. 3), the data clearly shows this Arrhenian trend and can be described by the following equation:

$$D = D_0 e^{-\frac{E_A}{RT}} \quad (2)$$

where D is the diffusion coefficient (m²/s), D_0 is the pre-exponential factor, E_A the activation energy (J/mol), R the universal gas constant (8.3145 J mol⁻¹ K⁻¹), and T is the temperature (K). The characteristic parameters describing the diffusivity behavior of each halogen in a specific melt composition are D_0 and E_A which are mathematically represented by the y-axis intercept and the slope of the trendline in the Arrhenius diagram, respectively. For the calculation of the characteristic Arrhenius parameters, Eq. (2) was linearized to the form

$$\log(D) = -\frac{E_A}{\ln(10)RT} + \log(D_0) \quad (3)$$

and fitted to all available data (EPMA + SIMS) of each starting material using the nonlinear least-squares method implemented with MATLAB. Where multiple profiles were measured on one sample and with the same method, the resulting diffusion coefficients were averaged to avoid a weighing effect during the Arrhenius fitting calculations. The results of all fits are illustrated in Fig. 3 and listed in Table 3. Due to very slow

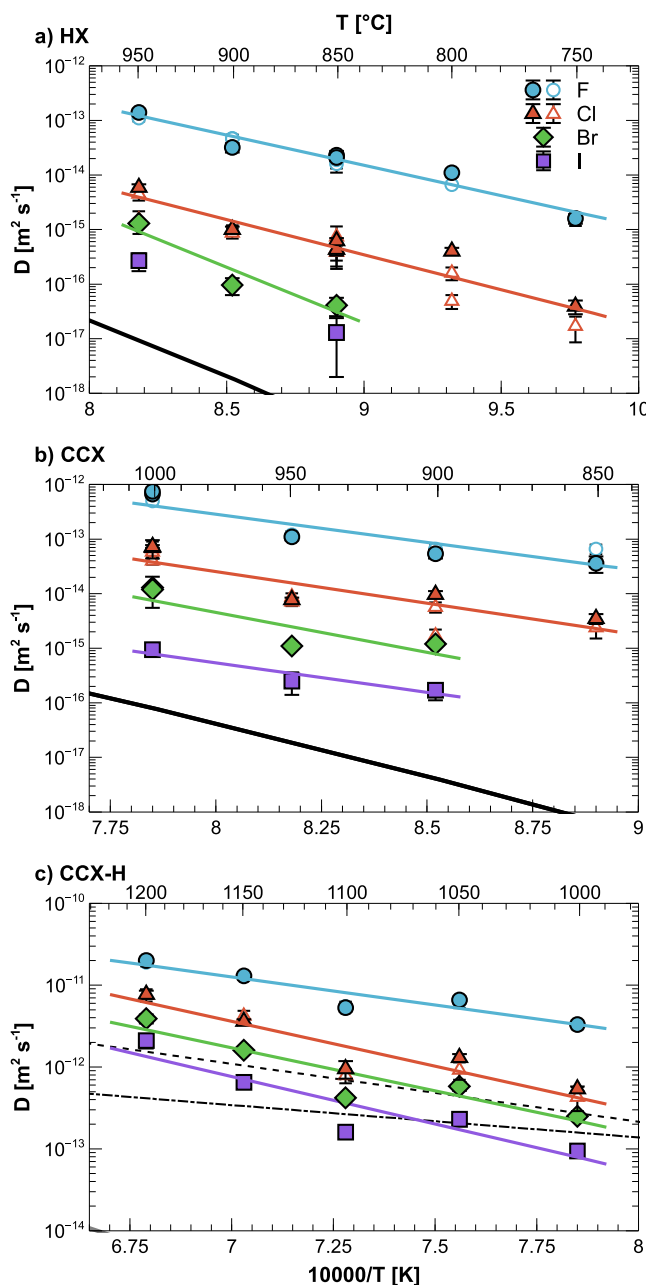


Fig. 3. Arrhenius diagrams of all investigated melt compositions illustrating the individual diffusion coefficients and the corresponding Arrhenius fits of all halogens. (a) Anhydrous HX melt. (b) Anhydrous CCX melt. (c) Hydrated CCX melt (~1.5 wt% H₂O). The bold black lines indicate the self-diffusivity of oxygen calculated with the Eyring-equation and based on the calculated viscosities of the anhydrous melt (Giordano et al., 2008). The dashed lines in (c) indicate calculated oxygen self-diffusion in rhyolite (dash-dot) and dacite (dashed) from (Zhang and Ni, 2010). Open symbols represent data based on EPMA analyses.

diffusion of I in the experiments of the HX series, only two datapoints yielded reliable results. Therefore, no Arrhenius parameters could be fitted for I diffusion in HX melt. Fitted with the data of the two anhydrous series, the results of the HX and CCX starting materials are similar, mostly yielding activation energies in the range of ~200–280 kJ/mol for all halogens, with an outlier of 390 kJ/mol for Br diffusion in HX melt. However, diffusion in HX melt generally comprises slightly higher activation energies than in CCX melt. The similarity is further represented by the parallel fit curves in the Arrhenius diagrams (Fig. 3). However, in the HX series it is apparent that F is significantly faster than

all other halogens which is represented by a gap of 1.5–2 orders of magnitude between the fit lines of F and Cl, while Cl and Br are within about 1.5 orders of magnitude. In comparison, the data of the CCX series shows more equally spaced Arrhenius fits of the halogens spanning an overall similar range of diffusivities compared to the HX experiments.

The data of the hydrous series shows the same ordering of diffusivities, with F being the fastest and I being the slowest, but spanning a narrower range of diffusivities among all halogens. In the Arrhenius diagram this is represented by the more closely spaced fit curves compared to the anhydrous data (Fig. 3). Activation energies are similar to the anhydrous series, except for F whose E_A is only 131 kJ/mol in the hydrous case compared to 198–213 kJ/mol in the anhydrous experiments (Table 3).

3.5. H₂O content in CCX-H experiments

The experimental products of the CCX-H series show a range of 1.5–2 wt% H₂O (Table 2). Most of the hydrous experiments suffered from water loss to some extent, which was indicated by increasing totals towards one end of the diffusion profile recognized in the EPMA results (Fig. 1) and confirmed by SIMS analyses (Figs. 2, S1). The use of CH₄ in the pressure medium helped to reduce this issue but did not resolve it completely. Interestingly, water was only lost on the halogen-depleted side of the diffusion couple leading to a weak, mostly linear H₂O-concentration gradient over the length of the diffusion couple. Experiments comprising significant water loss were discarded, however, small losses were considered negligible with regard to diffusivity. This is particularly true considering that the transition between high and low halogen concentration in most cases is relatively narrow, especially relative to the short diffusion lengths of the slower diffusing halogens. Over this narrow range the H₂O concentration can be considered to be constant within error. Due to this issue, we have calculated the average H₂O-concentration over the length of the transition zone of each hydrous diffusion profile and reported it with other relevant data in Table 2.

It is important to note that the weak inhomogeneities in H₂O concentrations within and upon the different samples could influence local diffusivities and thus may have induced some uncertainty on the calculated diffusion coefficients. While no distortion of halogen diffusion profiles was recognized during data fitting (such would be the case if diffusion was locally accelerated or retarded due to higher or lower local H₂O concentrations), these uncertainties due to the experimental limitations have to be considered in the application of the derived coefficients.

4. Discussion

4.1. Halogen diffusion mechanisms

Diffusivity and the mechanism of halogen diffusion are both strongly dependent on the composition and internal structure of the host melt. In the case of aluminosilicate melts a vast range of compositions are present in nature and structural melt parameters such as the degree of polymerization show an accordingly wide range. Arrhenius parameters of halogen diffusion have been determined for a range of different melt compositions and illustrate the strong compositional dependence of halogen diffusion (Watson and Bender, 1980; Dingwell and Scarfe, 1984; Dingwell and Scarfe, 1985; Bai and Koster van Groos, 1994; Alletti et al., 2007; Balcone-Boissard et al., 2009; Böhm and Schmidt, 2013; Fortin et al., 2017; Yoshimura, 2018; Balcone-Boissard et al., 2020). Most of these studies studied F and Cl diffusion and only few have investigated Br diffusion. However, none of the available studies provide I diffusivity data. Hence the present study is the first to our knowledge.

Typically, the degree of polymerization, being a major compositional property of a melt, is characterized by the parameter of NBO/T, i.e., the ratio of non-bridging oxygen atoms over tetrahedrally coordinated ions (Mysen, 1988). The melts of the present study exhibit NBO/T values in

Table 3

Arrhenius parameters of all halogens and oxygen self-diffusion in all investigated melt compositions. D_0 is given in m^2/s and E_A is given in kJ/mol . Calculation of Eyring diffusivities is described in the text. The standard errors (SE) of E_A are calculated during the least-squares Arrhenius fitting.

	HX			CCX			CCX-H		
	D_0	E_A	SE	D_0	E_A	SE	D_0	E_A	SE
F	1.50×10^{-4}	212.7	12.6	5.11×10^{-5}	197.5	40.6	7.76×10^{-7}	131.0	16.5
Cl	1.24×10^{-4}	245.8	22.9	5.10×10^{-5}	222.6	45.8	1.74×10^{-4}	210.1	29.3
Br	4.97×10^{-1}	391.6	125.3	2.32×10^{-3}	279.8	185.5	3.97×10^{-5}	201.4	48.2
I	–	–	–	2.55×10^{-7}	207.4	73.7	1.02×10^{-4}	222.2	56.6
O_{Eyring}	6.9×10^{-1}	399.1	10.3	1.43×10^{-1}	375.5	8.6	–	–	–

the range of ~ 0.08 – 0.11 , calculated using the method of (Mysen, 1988) and splitting FeO_{tot} equally between Fe_2O_3 and FeO (Giordano et al., 2008). The NBO/T values are reported together with the bulk rock chemistry in Table 1.

The bond strength of an ionic species dissolved in melt generally increases with the charge of that species and inversely with size (Zhang et al., 2010). Halogens in the combined state (e.g., as a halide) typically have an univalent charge of -1 and are therefore comparably weakly bonded to other atoms, despite being very reactive. This means that halogens are relatively easily detached from their original site by breakage of the ionic bonds around a previously coordinated halogen ion before moving to a new site (Zhang et al., 2010). Additionally, even though the halogen group elements have the highest electronegativity of all elements in their respective periods, the significant within group variation in this parameter means that the bond strength should also vary accordingly. For example, F, being the most electronegative, should foster the highest bond strength of the halogens. Within this simplified chemical framework the diffusive “jump” can be envisioned to proceed by passing through an aperture formed by neighbouring ions. The size and stiffness of the aperture should generally be structurally controlled and relate to the polymerization of the melt and the specific coordination environment of the particular ion site, while the detachment rate should be controlled by ionic charge and size (Zhang et al., 2010). The size and number of the apertures are determined by the ions present in the melt and the resulting “free space” formed which is called the ionic porosity, which again should depend on the specific nearest neighbour environment. As such the effective ionic porosity for F should differ from that for Cl, Br, and I. Fluorine strongly bonds with aluminosilicate network as Al-F species and to a smaller degree as Si-F species (e.g., Zeng and Stebbins, 2000; Kiczinski and Stebbins, 2002; Dalou et al., 2015), while the larger halogens cluster with Ca and Na, with no evidence for the interaction with the network cations (Stebbins and Du, 2002; Sandland et al., 2004; Cochain et al., 2015). Generally, smaller ions such as F diffuse faster, because they can pass through apertures of various sizes and are therefore less sensitive to ionic porosity. Larger ions can only pass large apertures and their diffusion-rate is therefore structurally controlled and, hence, more sensitive to ionic porosity. This is typically the case for noble gases and monovalent ions (e.g., Henderson et al., 1985; Lux, 1987; Alletti et al., 2007) and was also confirmed for halogens by recent studies which showed that diffusion is negatively correlated with the ionic radius of the halogen in low NBO/T melts, i.e., in melts with a high degree of polymerization (rhyodacite/trachyte, NBO/T: ~ 0.08 , Feisel et al., 2019; Na- and K-phonolite, NBO/T: ~ 0.08 , Balcone-Boissard et al., 2020). In melts with higher NBO/T (lower degree of polymerization) halogen diffusion typically comprises only weak correlation with the ionic radius. Alletti et al. (2007) suggested that halogen diffusion in a basaltic melt (NBO/T ~ 0.5) is mostly independent of “free space” in the melt structure but instead occurs by exchange mechanisms that are predominantly controlled by the preservation of local charge balance, similar to the diffusion of divalent and trivalent cations (Henderson et al., 1985). This means that in this kind of melt movement of halogens is increasingly rate-limited by the charge-controlled detachment process.

The present study complements the data of Feisel et al. (2019) by

including all new SIMS analyses which also cover Br and I in two different highly polymerized melts (HX: NBO/T ~ 0.08 ; CCX: NBO/T ~ 0.08 – 0.11). Fig. 4 illustrates the diffusivity of the halogens in different melt compositions relative to their ionic radii at 1250°C . The data of ionic radii used here are those published for typical univalent halogen species in a 6-fold coordination environment (Shannon, 1976). Even though no detailed information on the actual coordination environment of halogens in the experimental silicate glasses are available for validation we consider these values to be representative of the relative ionic radii and therefore a relevant baseline for the qualitative interpretation of melt structural processes. The data of Alletti et al. (2007) are included as a reference of a weakly polymerized melt and the data of studies performed at lower temperatures were calculated based on the published Arrhenius parameters. The results of the present study and especially those of Br and I confirm the strong influence of the ionic radius on diffusivity in polymerized anhydrous melts. The difference between F and Cl is particularly pronounced for most anhydrous studies, yielding a significant negative slope between the two in the diagram (Fig. 4). For the anhydrous CCX melt the slope increases from Br to I. This stepwise correlation of ionic radius and diffusivity is recognized for all polymerized melts that were analyzed for Br (and I). We interpret this behavior to show that the ionic porosity of the melt is limited to distinct aperture sizes dictated by the melt structure and the respective coordination environments of the different halogens. The fact that Cl and Br seem to have a similar diffusivity in anhydrous phonolite (Balcone-Boissard et al., 2009) regardless of their different ionic radii suggests that Cl and Br move through similarly sized apertures in this melt. By contrast, in the CCX melt, Br cannot move through the same apertures as Cl due to its size, resulting in its lower diffusivity. Likewise, the I ion is too large to pass these aperture sizes and can diffuse only in the vicinity

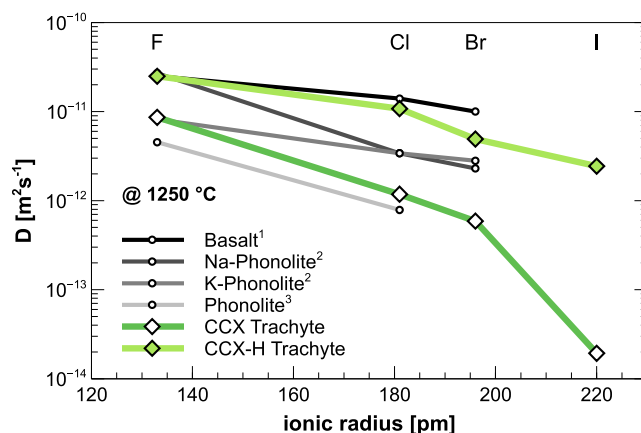


Fig. 4. Halogen diffusivity at 1250°C of the melts of this and other published studies plotted relative to the ionic radius of the respective halogen. All data are for anhydrous compositions except the hydrous data of the present study. Diffusivities at 1250°C were calculated from the respective Arrhenius parameters of each composition and halogen. Data from ¹Alletti et al., (2007); ²Balcone-Boissard et al., (2009) and Balcone-Boissard et al., (2020); ³Böhm and Schmidt, (2013).

of ions that allow the formation of larger openings between sites. F, being the fastest diffuser among all of the halogens, can move through both small openings and all the larger apertures that are used by Cl, Br, and I in a polymerized anhydrous melt. Our diffusivity data further supports the idea that fluorine can bond directly to aluminosilicate network cations (Mysen and Virgo, 1985; Schaller et al., 1992; Zeng and Stebbins, 2000) while the larger halogens coordinate with alkali and earth alkali cations (Stebbins and Du, 2002; Sandland et al., 2004; Louvel et al., 2020; Thomas et al., 2023). Within this framework the stepwise change in diffusivity from Cl to F seen in the low-alkali trachyte CCX may reflect lower detachment rates of small anions bonded strongly to a small cation of high-field strength. In consequence, fluorine diffusivity is slower than extrapolation of the trend defined by I, Br and Cl. For the larger Cl, Br and I anions bonded weakly to large cations, a higher detachment rate can be expected and the diffusivity should strongly depend on ionic size and the availability of suited coordination environments (e.g., Ca and Na). Fluorine diffusivity in more alkali rich melts like our HX and CCX trachyte or phonolite are less sensitive to this hampering effect. Again, this agrees with the idea that in alkali-rich aluminosilicate melts fluorine sites that are coordinated by Na and Ca, comparable to sites hosting Cl or Br, become increasingly important.

4.2. The effect of H₂O on diffusion

The hydrous experiments (~1.5 wt% H₂O) generally yield high diffusivities which span a range of only 1–2 orders of magnitude among the different halogens (Fig. 3). This restricted range of diffusivities contrasts those of the anhydrous CCX melt which displays 3–4 orders of magnitude variation. For better comparison to the anhydrous results, the Arrhenius parameters of the anhydrous CCX series were used to calculate hypothetical anhydrous diffusivities in the temperature range of the hydrous experiments and plotted in an Arrhenius diagram together with the hydrous Arrhenius fits (Fig. 5). The calculated anhydrous values are consistently lower than the hydrous data. While the difference for F is only ~0.2 log units at high *T* (1200 °C) and ~0.8 log units at low *T* (1000 °C), the difference for the larger halogens is more pronounced. Cl is ~1 log unit, Br ~0.5–1.5 log units and I ~2 log units faster in hydrous compared to dry melt. These results highlight the strong influence of H₂O on halogen diffusivity in the high silica melts of this study. These findings are in contrast to the those of Balcone-Boissard et al., (2020), who showed that the addition of up to 2.65 wt% H₂O exerts only minor influence on Br diffusion in phonolitic melts; a fact which further underlines the strong compositional dependence of halogen diffusion.

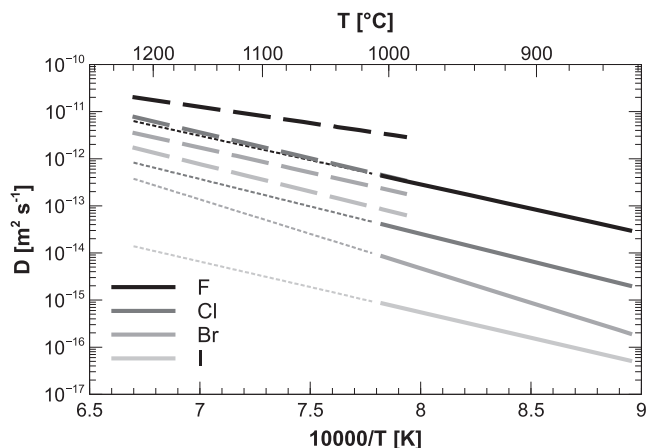


Fig. 5. Comparative Arrhenius diagram of halogen diffusion in anhydrous and hydrous (1.5 wt% H₂O) trachytic melt determined in this study. Solid lines represent diffusion in anhydrous melt and dotted lines indicate extrapolation to higher temperatures. Long-dashed lines represent diffusion in hydrous melt (1.5 wt% H₂O).

The increase in diffusivity in the melts of this study indicates a change in the diffusion mechanism that is likely caused by the modification of the melt structure due to the addition of H₂O. This effect is also indicated in Fig. 4, where the strong correlation of diffusivity with the ionic radii observed in the anhydrous melts is highly attenuated for the hydrous case. Indeed, the hydrous data is more similar to those of basalt confirming that water effectively lowers the degree of polymerization of the melt. In doing so, the rate-limiting influence of melt structural apertures is reduced which makes the process of detachment more relevant as a diffusion-rate-limiting factor. Interestingly, the slope between Cl and Br increases in the hydrous melt similar to the behavior in the anhydrous CCX melt. At the relatively low water contents of ~1.5 wt% used in the present study, the majority of the added H₂O is expected to be dissociated to form hydroxyl (OH⁻) in the melt (e.g., Silver et al., 1990; Ihinger et al., 1999). The experimental results indirectly show that hydroxyl effectively depolymerizes the melt and allows for faster halogen diffusion. However, even in the hydrated melt, halogen diffusion is still somewhat correlated with the ionic radii. This may indicate that for the given added water content (~1.5 wt%) the melt structure is still polymerized enough to assert some control on the aperture-limited jumping processes, mainly affecting larger ions. We speculate that diffusivities will increase even more and may become more equal among the halogen species with increased water content and concomitant increased depolymerization.

Another notable distinction between anhydrous and hydrous melt is the change in the activation energy, *E_A*, of F diffusion, which is lowered from 198 to 131 kJ mol⁻¹, while the *E_A* of the other halogens are only weakly affected (Table 3). That is, F diffusion becomes less sensitive to temperature in hydrous melts, which is apparent in the comparably shallow slope of the F Arrhenius fit in Figs. 3c and 5. As already concluded from the observation that F diffusion is less strongly enhanced in the hydrous melt, compared to the other halogens, F diffusion appears only weakly sensitive to the melt structure and is more strongly controlled by the detachment process. F is known to substitute for bridging oxygen in Si—O—Al units (e.g., Mysen and Virgo, 1985) and preferably coordinates with Al or to some extent with Si (e.g., Zeng and Stebbins, 2000; Kiczinski and Stebbins, 2002; Liu and Nekvasil, 2002), while Cl and Br prefer to coordinate in larger sites with mainly Na and Ca (Sandland et al., 2004; Dalou et al., 2015; Cassidy et al., 2022). Similarly, OH⁻ typically replaces oxygen bonds of the Si—O network (Mysen et al., 1980). Consequently, the addition of H₂O and the concomitant formation of OH⁻ in the melt must influence the preferred bonding environment of F in the silicate network. Here, we interpret the change in activation energy of F to reflect that the rate of detachment from its site is enhanced by the replacement of F with OH⁻. This way more F is available for diffusion compared to the anhydrous case, which in turn suggests that F diffusion becomes less sensitive to temperature (i. e., lower activation energy) under hydrous conditions. Consequently, we speculate that the introduction of water has a twofold effect on the halogen diffusion mechanism: (1) The resulting decrease in the degree of polymerization generally promotes halogen diffusivities by increasing the ionic porosity; (2) The strong effect on the activation energy of F is interpreted to be due to OH⁻ directly affecting the bonding environment of F. Clearly, these explanations are qualitative, and therefore meant to suggest possible microscale chemical processes that might explain our macroscopic observations. Testing these ideas could benefit from appropriate imaging experiments (e.g., Schaller et al., 1992; Zeng and Stebbins, 2000; Mysen et al., 2004) that may isolate the relevant coordination and bonding environments of the halogens, with implications for their bond strengths in natural silicate melt.

4.3. Halogen diffusion and viscosity

Oxygen self-diffusion is commonly seen as a solid estimate of the structurally defined lower limit of diffusion rates in silicate melts (Oishi et al., 1975; Shimizu and Kushiro, 1984; Dingwell, 1990; Leshner, 2010;

Zhang and Ni, 2010) and appears closely related to anhydrous melt viscosity via the Eyring equation (Glasstone et al., 1941; Dingwell, 1990; Zhang and Ni, 2010). Calculated oxygen self-diffusivity of our anhydrous samples using viscosity data derived from the model of Giordano et al. (2008) are included in Fig. 3.

Diffusion of all four halogens in the dry melt is at least 1 order of magnitude faster than the calculated oxygen self-diffusion (Fig. 3), indicating that the silicate network behaves as in quasi-static structural sites relative to the diffusing halogen ion; therefore, diffusion may only be affected weakly by self-diffusion of the silicate network. Notably, iodine diffusion is the slowest of the halogens and thus closest to the calculated Eyring diffusion. The steeper slope of the Eyring diffusivity compared to the slope of the halogen fits in the Arrhenius diagrams (Fig. 3) suggests that with increasing temperature the jump frequency of iodine may approach that of the Si–O bonds in the silicate structure and the network surrounding iodine may no longer be viewed as quasi-static. With increasing temperature, iodine diffusion might therefore be enhanced by the cooperative rearrangement of the local silicate structure as oxygen diffuses.

The activation energy of diffusion, i.e., the slopes of the Arrhenius fits of the other halogens (Fig. 3) likewise indicate that all fits will meet the lower limit of oxygen self-diffusion at higher temperatures. Consequently, at sufficiently high temperatures (i.e., sufficiently low viscosity), all halogens will move with the same frequency as the silicate network, hence, diffusion will be the same for all halogens, being determined by the jump frequency of the structural movement of the Si–O bonds, broadly consistent with the conclusions of Dingwell (1990).

The indicated oxygen self-diffusivities in Fig. 3 are considered to represent the lower limit of possible values as they are based on the halogen-depleted melt compositions. In F bearing melts, like those of the enriched diffusion couple halves, the viscosity can be significantly reduced due to the depolymerizing effect of F (e.g., Dingwell et al., 1985; Giordano et al., 2008), which will in turn yield higher calculated oxygen self-diffusivities. For the melts used in this study, the F-bearing melts yield Eyring diffusivities of up to 1 order of magnitude higher than the F-depleted melts, approaching the derived diffusivities of iodine at the highest of the experimental temperatures. Therefore, during the experiments, the melt structural lower limit of halogen diffusion is expected to change upon diffusion of F. In the resulting F enriched melts, the halogen diffusivities might approach the Si–O jump frequency already at lower temperatures compared to the F-depleted case. Expanding on this idea, we speculate that when F diffusivity and the F-depleted Eyring diffusivity are within ~1 order of magnitude in Arrhenius space (i.e., at sufficiently high temperatures), diffusion of F into the depleted melt will enhance F diffusivity by decreasing the degree of polymerization. This would in turn result in a concentration dependent F diffusivity comparable to the case of H₂O (e.g., Behrens et al., 2004). However, it is unclear if the Eyring equation is valid for the case of F-enriched polymerized melts.

In case of the hydrous melt, the Eyring equation was shown to be inapplicable as it under-estimates oxygen-diffusion by 3–4 orders of magnitude in rhyolitic melt (Behrens et al., 2007). In this case, oxygen no longer moves solely by self-diffusion but is mainly transported by the diffusion of molecular H₂O in the melt (Behrens et al., 2007; Zhang and Ni, 2010) which shows that the structural limit of diffusion rates in hydrous melt can no longer be described by the self-diffusion of oxygen.

In an attempt to define a lower limit of diffusion rates in the hydrous melt of the present study, calculated oxygen self-diffusivities of rhyolite and dacite (Tables 4 and 5 of Zhang and Ni, (2010)) have been included in Fig. 3c. However, these predicted self-diffusivities are faster than the experimentally constrained diffusivities of Br and I over a large range of the investigated temperatures. This is interpreted to indicate that in a slightly depolymerized melt of sufficiently large ionic porosity, the jumps of Si–O bonds no longer define the lower limit of transport rates but that the diffusive characteristics may be mostly determined by the

ionic charge and radius.

4.4. Halogen diffusion in different silicate melt compositions

The diffusion data presented in this study expands the database of halogen diffusion in silicic melt and, owing to the silica-rich nature of the melt and the experimental approach used, significantly extends it to lower temperatures and lower diffusivities than discussed by most of the previous studies in that field. In Fig. 6, the general results of the recent study are compared to the findings of previous studies on halogen diffusion in a broad range of melt compositions. The Arrhenius fits of F in anhydrous melt determined in this study (Fig. 6a) comprise a similar slope to those of basalt and K-rich phonolite (Alletti et al., 2007; Balcone-Boissard et al., 2009) which suggests similar diffusivities of F in silicic melt at comparably high temperatures. This supports the idea that F diffusion is less influenced by ionic porosity and the melt structure, but is instead largely controlled by the detachment process which is mainly temperature dependent in anhydrous melt. At hydrous conditions, the activation energies of F diffusion decrease and are similar to those of F diffusing in other hydrous low-silica melts.

The Arrhenius fits of Cl diffusion in anhydrous silicic melt of this study (Fig. 6b) comprise similar activation energies to those of Cl diffusion in basalt and Na-phonolite (Alletti et al., 2007; Balcone-Boissard et al., 2009). However, unlike with F diffusion, when extrapolating the fits of Cl to higher temperatures, they still plot significantly below those of basalt and Na-phonolite indicating that Cl diffusion is more strongly limited by the polymerized nature of the melt. The hydrous melt instead reveals enhanced Cl diffusivities that are similar to those in anhydrous basalt.

Due to the scarcity of Br and especially I diffusion data, all previous and the recent data of both halogens are presented together in Fig. 6c. The activation energies of both halogens are very similar in each melt but are different between the different melts, which we attribute to the slight compositional variation, especially in Na₂O. Even under high temperature conditions, Br and I in anhydrous silicic melt are still significantly slower diffusers than Br in other, more primitive melts such as basalt or phonolite (Alletti et al., 2007; Balcone-Boissard et al., 2020). However, at hydrous conditions diffusivities of Br and I in silicic melt increase significantly and approach those of Br in the low-silica melts.

4.5. Implications

These novel data are highly relevant for the better understanding of halogen mobility in magmatic processes and illustrate the diffusive variability between different melt compositions and among the halogens themselves (Figs. 3–5). Highly different halogen diffusivities in silicic melts imply that mass transport of slower diffusing halogen species from the melt into a bubble is relatively limited and may lead to depletion of these elements in the gas phase of a degassing volcano. Ultimately, this may result in diffusive fractionation of the residual melt, which may accumulate the slower diffusing halogens in the melt, while the faster diffusing halogens such as F and Cl can leave more efficiently. This process may be monitored remotely by time-series analyses of volcanic degassing. Additionally, using these data, the process may be modelled to help forecast typical volcanic degassing behaviour. However, for the modelling to be representative, additional melt specific halogen properties such as vapour-melt or crystal-melt partition coefficients need to be known. In a scenario of a slowly degassing static magma body, it is expected that certain halogen ratios are reached and maintained in the gas phase during degassing, which will deviate from the static ratio when magma ascends. Likewise, different rates of mass transport among the halogens may cause zoning during crystal-growth or non-representative compositions of trapped melt-inclusions (e.g., Baker et al., 2005).

To apply diffusivity data to determine timescales of volcanological processes it is crucial to understand the diffusion behavior of the

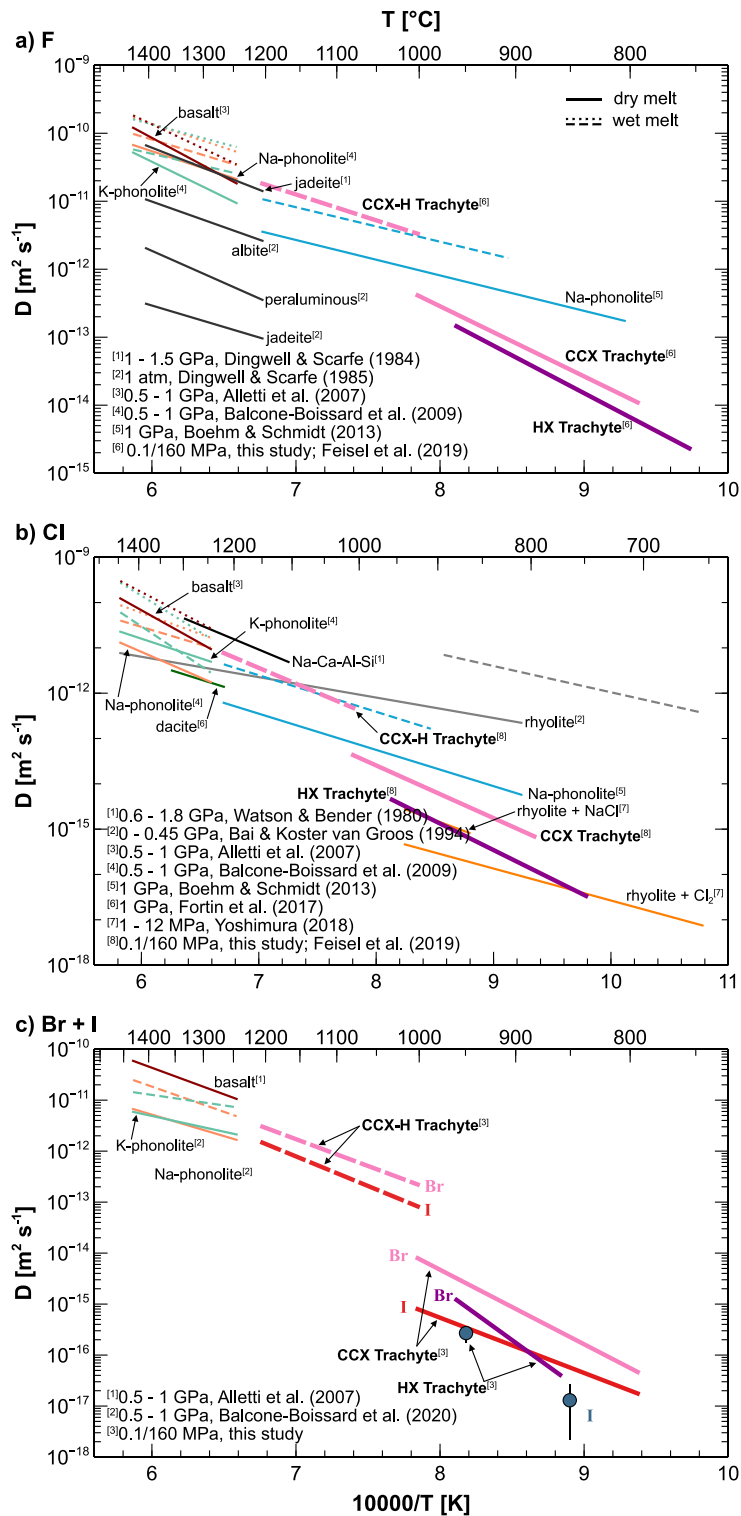


Fig. 6. Arrhenius diagrams showing a comparison of the recent data to those from previous studies on halogen diffusion in a range of silicate melt compositions. (a) Fluorine diffusion, (b) Chlorine diffusion and (c) Bromine and Iodine diffusion. Solid and dashed lines of the same colour within one diagram correspond to the hydrous and anhydrous case of the same melt composition, respectively.

investigated species in the respective melt composition, including all relevant parameters, such as the H₂O content of the melt. For example, Yoshimura et al., (2019) analyzed Cl contents in silicate magma and determined the timescales of degassing by means of Cl diffusivity. As the present data shows, Cl diffusivity may vary by more than 1 order of magnitude depending on the water content (0–1.5 wt%) which would induce high uncertainty to the determined timescales if the water

content was not considered in sufficient detail. These examples underline the relevance of melt specific halogen diffusion data for the application of these data in interpreting geochemical processes.

5. Conclusions

The diffusion characteristics of four halogens in silicic melts were

determined experimentally under anhydrous and hydrous conditions and over a temperature range relevant for magmatic processes (750–1200 °C). The results are consistent in that F is the fastest diffusing halogen and diffusivity decreases with increasing ionic radius indicating that diffusivity is highly dependent on the melt structure and therefore melt composition. Halogen diffusion covers a range of 3–4 orders of magnitude in silica-rich anhydrous melt, but diffusivities increase dramatically when water is added. The diffusivity increase due to the addition of water is most pronounced for the largest of the halogens and thus, the slowest diffusing halogen iodine. The effect of added water is weaker for the smaller halogens, leading to an overall diffusive range of only 1–2 orders of magnitude among all halogens. While the temperature dependence in terms of activation energies of Cl, Br and I diffusion is similar in the dry and wet case (~200–290 kJ/mol), E_A of F is reduced by about 35 % in hydrous (~131 kJ/mol) compared to anhydrous melt (~200 kJ/mol). This is interpreted to indicate that F diffusion is less sensitive to ionic porosity and more strongly dependent on the ionic detachment, the process of which is impacted due to the changed bonding environment of F upon the addition of H₂O to the melt.

This study represents a significant contribution to the experimental database of halogen diffusion in natural silicate melts, and to our knowledge, is the first to include coherent results on iodine diffusion. The new data are highly relevant for the better understanding of halogen mobility in magmatic processes. Our results suggest that diffusive fractionation of faster diffusing components such as H₂O and the halogens, could occur during bubble formation in a weakly water-enriched magma during slow magma ascent (e.g., Watson, 2017). Modelling of different magma ascent and bubble growth scenarios using the proposed diffusion parameters may help to characterize possible halogen fractionation trends during volcanic unrest.

Declaration of Competing Interest

The authors declare that they have no known competing financial interests or personal relationships that could have appeared to influence the work reported in this paper.

Data availability

Data are available through Mendeley Data at <http://dx.doi.org/10.17632/n22zvrw5z2.1>.

Acknowledgements

We thank N. Groschopf and S. Buhre for their guidance during electron microprobe analyses. T. Häger is thanked for access to the precision diamond wire saw. The help of B. Scheu, U. Kueppers, and K.-U. Hess with pre-synthesis sample preparation at LMU Munich is appreciated. This research was part of the Ph.D. thesis of Y. Feisel at the Johannes Gutenberg-University, Mainz. It was supported by a fellowship of the Gutenberg Research College of the Johannes Gutenberg-University of Mainz to D.B. Dingwell, who also acknowledges the support of ERC2018 ADV Grant 834225 (EAVESDROP).

We thank S.K. Lee and J. Catalano for the editorial handling and M. Holycross and two anonymous reviewers for their comprehensive reviews of the manuscript.

Appendix A. Supplementary material

Backscattered images of all samples, all acquired diffusion profile data and the SIMS analysis conditions at the different facilities are reported in the Appendix. Supplementary material to this article can be found online at <https://doi.org/10.1016/j.gca.2023.07.008>.

References

- Aiuppa, A., Baker, D.R., Webster, J.D., 2009. Halogens in volcanic systems. *Chem. Geol.* 263, 1–18.
- Alletti, M., Baker, D.R., Freda, C., 2007. Halogen diffusion in a basaltic melt. *Geochim. Cosmochim. Acta* 71, 3570–3580.
- Alloway, B.V., Pearce, N.J.G., Villarosa, G., Outes, V., Moreno, P.I., 2015. Multiple melt bodies fed the AD 2011 eruption of Puyehue-Cordón Caulle, Chile. *Sci. Rep.* 5, 1–8.
- Baasner, A., Schmidt, B.C., Webb, S.L., 2013. Compositional dependence of the rheology of halogen (F, Cl) bearing aluminosilicate melts. *Chem. Geol.* 346, 172–183.
- Bai, T.B., Koster van Groos, A.F., 1994. Diffusion of chlorine in granitic melts. *Geochim. Cosmochim. Acta* 58, 113–123.
- Baker, D.R., Balcone-Boissard, H., 2009. Halogen diffusion in magmatic systems: Our current state of knowledge. *Chem. Geol.* 263, 82–88.
- Baker, D.R., Freda, C., Brooker, R.A., Scarlato, P., 2005. Volatile diffusion in silicate melts and its effects on melt inclusions. *Ann. Geophys.* 48.
- Balcone-Boissard, H., Baker, D.R., Villemant, B., Boudon, G., 2009. F and Cl diffusion in phonolitic melts: Influence of the Na/K ratio. *Chem. Geol.* 263, 89–98.
- Balcone-Boissard, H., Villemant, B., Boudon, G., 2010. Behavior of halogens during the degassing of felsic magmas. *Geochim. Geophys. Geosyst.* 11.
- Balcone-Boissard, H., Baker, D.R., Villemant, B., Cauzid, J., Boudon, G., Delouie, E., 2020. Br diffusion in phonolitic melts: Comparison with fluorine and chlorine diffusion. *Am. Mineral.* 105, 1639–1646.
- Behrens, H., Zhang, Y., Xu, Z., 2004. H₂O diffusion in dacitic and andesitic melts. *Geochim. Cosmochim. Acta* 68, 5139–5150.
- Behrens, H., Zhang, Y., Leschik, M., Wiedenbeck, M., Heide, G., Frischat, G.H., 2007. Molecular H₂O as carrier for oxygen diffusion in hydrous silicate melts. *Earth Planet. Sci. Lett.* 254, 69–76.
- Bobrowski, N., Hönninger, G., Galle, B., Platt, U., 2003. Detection of bromine monoxide in a volcanic plume. *Nature* 423, 273–276.
- Bobrowski, N., von Glasow, R., Aiuppa, A., Inguaggiato, S., Louban, I., Ibrahim, O.W., Platt, U., 2007. Reactive halogen chemistry in volcanic plumes. *J. Geophys. Res. Atmos.* 112.
- Böhm, A., Schmidt, B.C., 2013. Fluorine and chlorine diffusion in phonolitic melt. *Chem. Geol.* 346, 162–171.
- Bureau, H., Keppler, H., Métrich, N., 2000. Volcanic degassing of bromine and iodine: Experimental fluid/melt partitioning data and applications to stratospheric chemistry. *Earth Planet. Sci. Lett.* 183, 51–60.
- Cadoux, A., Scaillet, B., Bekki, S., Oppenheimer, C., Druitt, T.H., 2015. Stratospheric Ozone destruction by the Bronze-Age Minoan eruption (Santorini Volcano, Greece). *Sci. Rep.* 5, 1–12.
- Cassidy, M., Iveson, A.A., Humphreys, M.C.S., Mather, T.A., Helo, C., Castro, J.M., Ruprecht, P., Pyle, D.M., Eimf, 2022. Experimentally derived F, Cl, and Br fluid/melt partitioning of intermediate to silicic melts in shallow magmatic systems. *Am. Mineral.* 107, 1825–1839.
- Castro, J.M., Schipper, C.I., Mueller, S.P., Militzer, A.S., Amigo, A., Parejas, C.S., Jacob, D., 2013. Storage and eruption of near-liquidus rhyolite magma at Cordón Caulle, Chile. *Bull. Volcanol.* 75, 1–17.
- Castro, J.M., Cordonnier, B., Schipper, C.I., Tuffen, H., Baumann, T.S., Feisel, Y., 2016. Rapid laccolith intrusion driven by explosive volcanic eruption. *Nat. Commun.* 7, 13585.
- Cochain, B., Sanloup, C., de Grouchy, C., Crépinson, C., Bureau, H., Leroy, C., Kantor, I., Irifune, T., 2015. Bromine speciation in hydrous silicate melts at high pressure. *Chem. Geol.* 404, 18–26.
- Crank, J., 1975. *The Mathematics of Diffusion*. Clarendon-Oxford, London.
- Dalou, C., Le Losq, C., Mysen, B.O., Cody, G.D., 2015. Solubility and solution mechanisms of chlorine and fluorine in aluminosilicate melts at high pressure and high temperature. *Am. Mineral.* 100, 2272–2283.
- Dingwell, D.B., 1990. Effects of structural relaxation on cationic tracer diffusion in silicate melts. *Chem. Geol.* 82, 209–216.
- Dingwell, D.B., Hess, K.U., 1998. Melt viscosities in the system Na-Fe-Si-O-F-Cl: contrasting effects of F and Cl in alkaline melts. *Am. Mineral.* 83, 1016–1021.
- Dingwell, D.B., Scarfe, C.M., 1984. Chemical diffusion of fluorine in jadeite melt at high pressure. *Geochim. Cosmochim. Acta* 48, 2517–2525.
- Dingwell, D.B., Scarfe, C.M., 1985. Chemical diffusion of fluorine in melts in the system Na₂O - Al₂O₃ - SiO₂. *Earth Planet. Sci. Lett.* 73, 377–384.
- Dingwell, D.B., Scarfe, C.M., Cronin, D.J., 1985. The effect of fluorine on viscosities in the system Na₂O - Al₂O₃ - SiO₂: implications for phonolites, trachytes and rhyolites. *Am. Mineral.* 70, 80–87.
- Dolejš, D., Baker, D.R., 2007a. Liquidus equilibria in the system K₂O - Na₂O - Al₂O₃ - SiO₂ - F₂O₁ - H₂O to 100 MPa: I. Silicate-fluoride liquid immiscibility in anhydrous systems. *J. Petrol.* 48, 785–806.
- Dolejš, D., Baker, D.R., 2007b. Liquidus equilibria in the system K₂O - Na₂O - Al₂O₃ - SiO₂ - F₂O₁ - H₂O to 100 MPa: II. Differentiation paths of fluorosilicic magmas in hydrous systems. *J. Petrol.* 48, 807–828.
- Dolejš, D., Zajac, Z., 2018. Halogens in Silicic Magmas and Their Hydrothermal Systems. In: Harlow, D.E., Aranovich, L.Y. (Eds.), *The Role of Halogens in Terrestrial and Extra-Terrestrial Geochemical Processes*. Springer-Verlag, Cham, pp. 431–543.
- Farcy, B.J., Gross, J., Carpenter, P., Hicks, J., Filiberto, J., 2016. Effect of chlorine on near-liquidus crystallization of olivine-phyric shergottite NWA 6234 at 1 GPa: Implication for volatile-induced melting of the Martian mantle. *Meteorit. Planet. Sci.* 51, 2011–2022.
- Feisel, Y., Castro, J.M., Dingwell, D.B., 2019. Diffusion of F and Cl in dry rhyodacitic melt. *Am. Mineral.* 104, 1689–1699.

- Feisel, Y., Castro, J.M., Helo, C., Dingwell, D.B., 2022. The effect of halogens (F, Cl) on the near-liquidus crystallinity of a hydrous trachyte melt. *Am. Mineral.* 107, 1007–1017.
- Filiberto, J., Wood, J., Dasgupta, R., Shimizu, N., Le, L., Treiman, A.H., 2012. Effect of fluorine on near-liquidus phase equilibria of an Fe-Mg rich basalt. *Chem. Geol.* 312–313, 118–126.
- Filiberto, J., Dasgupta, R., Gross, J., Treiman, A.H., 2014. Effect of chlorine on near-liquidus phase equilibria of an Fe-Mg-rich tholeiitic basalt. *Contrib. Mineral. Petrol.* 168, 1–13.
- Fortin, M.A., Watson, E.B., Stern, R., 2017. The isotope mass effect on chlorine diffusion in dacite melt, with implications for fractionation during bubble growth. *Earth Planet. Sci. Lett.* 480, 15–24.
- Giordano, D., Russell, J.K., Dingwell, D.B., 2008. Viscosity of magmatic liquids: A model. *Earth Planet. Sci. Lett.* 271, 123–134.
- Glasstone, S., Laidler, K.J., Eyring, H., 1941. *The Theory of Rate Processes*. McGraw-Hill, New York.
- Gonnermann, H.M., Manga, M., 2007. The fluid mechanics inside a volcano. *Annu. Rev. Fluid Mech.* 39, 321–356.
- Henderson, P., Nolan, J., Cunningham, G.C., Lowry, R.K., 1985. Structural controls and mechanisms of diffusion in natural silicate melts. *Contrib. Mineral. Petrol.* 89, 263–272.
- Horwell, C.J., Le Blond, J.S., Michnowicz, S.A.K., Cressey, G., 2010. Cristobalite in a rhyolitic lava dome: Evolution of ash hazard. *Bull. Volcanol.* 72, 249–253.
- Ihinger, P.D., Zhang, Y., Stolper, E.M., 1999. The speciation of dissolved water in rhyolitic melt. *Geochim. Cosmochim. Acta* 63, 3567–3578.
- Jollands, M.C., 2020. Assessing analytical convolution effects in diffusion studies: Applications to experimental and natural diffusion profiles. *PLoS One* 15.
- Kiczanski, T.J., Stebbins, J.F., 2002. Fluorine sites in calcium and barium oxyfluorides: F-19 NMR on crystalline model compounds and glasses. *J. Non. Cryst. Solids* 306, 160–168.
- Leshar, C.E., 2010. Self-diffusion in silicate melts: Theory, observations and applications to magmatic systems. *Rev. Mineral. Geochem.* 72, 269–309.
- Liu, Y., Nekvasil, H., 2002. Si-F bonding in aluminosilicate glasses: Inferences from ab initio NMR calculations. *Am. Mineral.* 87, 339–346.
- Louvel, M., Cadoux, A., Brooker, R.A., Proux, O., Hazemann, J.-L., 2020. New insights on Br speciation in volcanic glasses and structural controls on halogen degassing. *Am. Mineral. J. Earth Planet. Mater.* 105, 795–802.
- Lowenstern, J.B., Bleick, H., Vazquez, J.A., Castro, J.M., Larson, P.B., 2012. Degassing of Cl, F, Li, and Be during extrusion and crystallization of the rhyolite dome at Volcán Chaitén, Chile during 2008 and 2009. *Bull. Volcanol.* 74, 2303–2319.
- Lux, G., 1987. The behavior of noble gases in silicate liquids: Solution, diffusion, bubbles and surface effects, with applications to natural samples. *Geochim. Cosmochim. Acta* 51, 1549–1560.
- Manning, D.A.C., 1981. The effect of fluorine on liquidus phase relationships in the system Qz-Ab-Or with excess water at 1 kb. *Contrib. Mineral. Petrol.* 76, 206–215.
- Marks, M.A.W., Kendrick, M.A., Eby, G.N., Zack, T., Wenzel, T., 2017a. The F, Cl, Br and I Contents of Reference Glasses BHVO-2G, BIR-1G, BCR-2G, GSD-1G, GSE-1G, NIST SRM 610 and NIST SRM 612. *Geostand. Geoanal. Res.* 41, 107–122.
- Marks, M.A.W., Kendrick, M.A., Wenzel, T., Eby, G.N., Zack, T., 2017b. Reply to ‘Comment on The F, Cl, Br and I Contents of Reference Glasses BHVO-2G, BIR-1G, BCR-2G, GSD-1G, GSE-1G, NIST SRM 610 and NIST SRM 612’. *Geostand. Geoanal. Res.* 41, 475–478.
- Mysen, B.O., 1988. *Structure and Properties of Silicate Melts*. Elsevier, Amsterdam.
- Mysen, B.O., Virgo, D., Harrison, W.J., Scarfe, C.M., 1980. Solubility mechanisms of H₂O in silicate melts at high pressures and temperatures: a Raman spectroscopic study: discussion. *Am. Mineral.* 65, 900–914.
- Mysen, B.O., Virgo, D., 1985. Interaction between fluorine and silica in quenched melts on the joins SiO₂ - AlF₃ and SiO₂ - NaF determined by raman spectroscopy. *Phys. Chem. Miner.* 12, 77–85.
- Mysen, B.O., Cody, G.D., Smith, A., 2004. Solubility mechanisms of fluorine in peralkaline and meta-aluminous silicate glasses and in melts to magmatic temperatures. *Geochim. Cosmochim. Acta* 68, 2745–2769.
- Oishi Y., Terai R., Ueda H., 1975. Oxygen diffusion in liquid silicates and relation to their viscosity. In: *Mass Transport Phenomena in Ceramics*, pp. 297–310.
- Pichavant, M., 1987. The Macusani glasses, SE Peru: evidence of chemical fractionation in peraluminous magmas. *Magmat. Process. Physicochem. Princ.* 359–373.
- Roberts, T., 2018. Ozone Depletion in Tropospheric Volcanic Plumes: From Halogen-Poor to Halogen-Rich Emissions. *Geosciences* 8, 68.
- Sandland, T.O., Du, L.-S., Stebbins, J.F., Webster, J.D., 2004. Structure of Cl-containing silicate and aluminosilicate glasses: A ³⁵Cl MAS-NMR study. *Geochim. Cosmochim. Acta* 68, 5059–5069.
- Schaller, T., Dingwell, D.B., Keppler, H., Knöller, W., Merwin, L., Sebald, A., 1992. Fluorine in silicate glasses: A multinuclear magnetic resonance study. *Geochim. Cosmochim. Acta* 56, 701–707.
- Schipper, C.I., Castro, J.M., Tuffen, H., James, M.R., How, P., 2013. Shallow vent architecture during hybrid explosive-effusive activity at Cordón Caulle (Chile, 2011–12): Evidence from direct observations and pyroclast textures. *J. Volcanol. Geotherm. Res.* 262, 25–37.
- Schipper, C.I., Castro, J., Kennedy, B., Christenson, B., Aiuppa, A., Alloway, B., Forte, P., Seropian, G., Tuffen, H., 2019. Halogen (Cl, F) release during explosive, effusive, and intrusive phases of the 2011 rhyolitic eruption at Cordón Caulle volcano (Chile). *Volcanica* 2, 73–90.
- Schipper, C.I., Rickard, W.D.A., Reddy, S.M., Saxey, D.W., Castro, J.M., Fougereuse, D., Quadir, Z., Conway, C., Prior, D.J., Lilly, K., 2020. Volcanic SiO₂-cristobalite: A natural product of chemical vapor deposition. *Am. Mineral.* 105, 510–524.
- Shannon, R.D., 1976. Revised effective ionic radii and systematic studies of interatomic distances in halides and chalcogenides. *Acta Crystallogr. Sect. A* 32, 751–767.
- Shea, T., Hammer, J.E., 2013. Oxidation in CSPV experiments involving H₂O-bearing mafic magmas: Quantification and mitigation. *Am. Mineral.* 98, 1285–1296.
- Shimizu, N., Kushiro, I., 1984. Diffusivity of oxygen in jadeite and diopside melts at high pressures. *Geochim. Cosmochim. Acta* 48, 1295–1303.
- Silver, L.A., Ihinger, P.D., Stolper, E., 1990. The influence of bulk composition on the speciation of water in silicate glasses. *Contrib. Mineral. Petrol.* 104, 142–162.
- Sisson, T.W., Grove, T.L., 1993. Experimental investigations of the role of H₂O in calc-alkaline differentiation and subduction zone magmatism. *Contrib. Mineral. Petrol.* 113, 143–166.
- Spilliaert, N., Métrich, N., Allard, P., 2006. S-Cl-F degassing pattern of water-rich alkali basalt: Modelling and relationship with eruption styles on Mount Etna volcano. *Earth Planet. Sci. Lett.* 248, 772–786.
- Stebbins, J.F., Du, L.-S., 2002. Chloride ion sites in silicate and aluminosilicate glasses: A preliminary study by 35Cl solid-state NMR. *Am. Mineral.* 87, 359–363.
- Surl, L., Donohoue, D., Aiuppa, A., Bobrowski, N., von Glasow, R., 2015. Quantification of the depletion of ozone in the plume of Mount Etna. *Atmos. Chem. Phys.* 15, 2613–2628.
- Szramek, L., Gardner, J.E., Larsen, J., 2006. Degassing and microlite crystallization of basaltic andesite magma erupting at Arenal Volcano, Costa Rica. *J. Volcanol. Geotherm. Res.* 157, 182–201.
- Thomas, R.W., Wade, J., Wood, B.J., 2023. The bonding environment of chlorine in silicate melts. *Chem. Geol.* 617, 121269.
- Thordarson, T., Larsen, G., 2007. Volcanism in Iceland in historical time: Volcano types, eruption styles and eruptive history. *J. Geodyn.* 43, 118–152.
- von Glasow, R., Bobrowski, N., Kern, C., 2009. The effects of volcanic eruptions on atmospheric chemistry. *Chem. Geol.* 263, 131–142.
- Watson, E.B., 2017. Diffusive fractionation of volatiles and their isotopes during bubble growth in magmas. *Contrib. Mineral. Petrol.* 172.
- Watson, E.B., Bender, J.F., 1980. Diffusion of cesium, samarium, strontium, and chlorine in molten silicate at high temperatures and pressures. *Geol. Soc. Am. Abstr. Programs* 12, 545.
- Weber, G., Castro, J.M., 2017. Phase petrology reveals shallow magma storage prior to large explosive silicic eruptions at Hekla volcano, Iceland. *Earth Planet. Sci. Lett.* 466, 168–180.
- Webster, J.D., Baker, D.R., Aiuppa, A., 2018. Halogens in mafic and intermediate-silica content magmas. In: Harlov, D.E., Aranovich, L.Y. (Eds.), *The Role of Halogens in Terrestrial and Extraterrestrial Geochemical Processes*. Springer-Verlag, pp. 307–430.
- Wiedenbeck, M., 2017. Comment on: The F, Cl, Br and I Contents of Reference Glasses BHVO-2G, BIR-1G, BCR-2G, GSD-1G, GSE-1G, NIST SRM 610 and NIST SRM 612. *Geostand. Geoanal. Res.* 41, 147–152.
- Yoshimura, S., 2018. Chlorine diffusion in rhyolite under low-H₂O conditions. *Chem. Geol.* 483, 619–630.
- Yoshimura, S., Kuritani, T., Matsumoto, A., Nakagawa, M., 2019. Fingerprint of silicic magma degassing visualised through chlorine microscopy. *Sci. Rep.* 9, 1–10.
- Zeng, Q., Stebbins, J.F., 2000. Fluoride sites in aluminosilicate glasses: High-resolution ¹⁹F NMR results. *Am. Mineral.* 85, 863–867.
- Zhang, Y., Ni, H., 2010. Diffusion of H, C, and O components in silicate melts. In: Zhang, Y., Cherniak, D.J. (Eds.), *Diffusion in Minerals and Melts*. Rev. Mineral. Geochem., Mineralogical Society of America, pp. 171–225.
- Zhang, Y., Ni, H., Chen, Y., 2010. Diffusion data in silicate melts. In: Zhang, Y., Cherniak, D.J. (Eds.), *Diffusion in Minerals and Melts*. Rev. Mineral. Geochem., Mineralogical Society of America, pp. 311–408.
- Zhang, Y., 2010. Diffusion in minerals and melts: Theoretical background. In: Zhang, Y., Cherniak, D.J. (Eds.), *Diffusion in Minerals and Melts*. Rev. Mineral. Geochem., Mineralogical Society of America, pp. 5–59.
- Zimova, M., Webb, S.L., 2007. The combined effects of chlorine and fluorine on the viscosity of aluminosilicate melts. *Geochim. Cosmochim. Acta* 71, 1553–1562.